Internal Radiative Feedback Triggers Global Collapse and Direct-Collapse Black Hole Formation in Metal-free Atomic-Cooling Haloes

Masaki Kiyuna[1]★, Sunmyon Chon[1,2,3], Kazuyuki Omukai[1] and Raffaella Schneider[3,4,5]
[1]Astronomical Institute, Graduate School of Science, Tohoku University, Aoba, Sendai 980-8578, Japan
[2]Max-Planck-Institut fur Astrophysik, Karl-Schwarzschild-Str. 1, D-85741 Garching, Germany
[3]Dipartimento di Fisica, "Sapienza" Università di Roma, Piazzale Aldo Moro 2, 00185 Roma, Italy
[4]Sapienza School for Advanced Studies, Viale Regina Elena 291, 00161 Roma, Italy
[5]INFN, Sezione Roma1, Dipartimento di Fisica, "Sapienza" Università di Roma, Piazzale Aldo Moro 2, 00185 Roma, Italy

arXiv:2610.03877v1 [astro-ph.GA] 2 Oct 2026

Accepted XXX. Received YYY; in original form ZZZ

ABSTRACT

The formation of heavy seed black holes from the collapse of supermassive stars (SMSs) is a promising pathway to the supermassive black holes (SMBHs). In the conventional direct-collapse scenario, however, SMS formation requires an extremely strong external far-ultraviolet (FUV) field to suppress H_2 cooling and fragmentation. Here, we use cosmological radiation-hydrodynamic simulations to show that SMSs can form in metal-free atomic-cooling haloes even under subcritical FUV backgrounds with $J_{21} = 1$–10^2. We follow the evolution for $\sim$ 1–2 Myr after the onset of star formation, including FUV and ionizing radiation from stars formed within the halo. Star formation proceeds through a characteristic two-stage evolution. H_2 cooling initially induces fragmentation and the formation of ordinary Pop III stars. Internal FUV radiation from these stars then photodissociates H_2 and suppresses further fragmentation, while the surrounding warm gas reservoir contracts under self-gravity and undergoes global collapse through atomic cooling. This collapse drives inflow rates of ~ 0.1–$1\ M_\odot\ yr^{-1}$ and produces rapidly accreting protostars that reach ~ 2–$6 \times 10^4\ M_\odot$ by the simulations end. Since rapid accretion is still ongoing, these objects are expected to grow to $\sim 10^5\ M_\odot$ SMSs and then form direct-collapse black holes (DCBHs). The global collapse is accompanied by clustered star formation, producing a compact, top-heavy stellar system around the SMSs. The estimated DCBH abundance, $n_{\rm DCBH} \sim 10^{-3}$–$10^{-2}$ cMpc^{-3}, is high enough to provide a plausible progenitor population for Little Red Dots and present-day SMBHs. Our results demonstrate that internal stellar feedback can trigger, rather than prevent, SMS formation, substantially relaxing the external FUV requirement for heavy-seed formation.

Key words: black hole physics – stars: black holes – quasars: supermassive black holes – stars: Population III – galaxies: formation.

1 INTRODUCTION

Recent JWST observations have revealed a growing number of candidate Population III (Pop III) galaxies with zero or extremely low metallicity around the epoch of reionization (Vanzella et al. 2023; Maiolino et al. 2024b, 2026; Morishita et al. 2025; Rusta et al. 2026; Nakajima et al. 2026). Pop III stars are generally thought to form in minihaloes with halo masses of $M_{\rm halo} \sim 10^5$–$10^6\ M_\odot$ at $z \sim 20$ (Bromm & Yoshida 2011; Klessen & Glover 2023), whereas Pop III galaxies are expected to form in more massive atomic-cooling haloes with $M_{\rm halo} \gtrsim 10^7$–$10^8\ M_\odot$ (Oh & Haiman 2002; Wise & Abel 2007; Greif et al. 2008; Bromm & Yoshida 2011). The deeper gravitational potentials of these haloes allow them to retain photoionized gas and sustain star formation despite stellar feedback, enabling the formation of the first galaxies (Greif et al. 2008; Bromm & Yoshida 2011; Pawlik et al. 2011, 2015; Hirano & Bromm 2017). To keep the gas pristine until the halo reaches the atomic-cooling scale, star formation in its progenitor minihaloes must be suppressed. FUV irradiation from nearby galaxies or the cosmic background provides a plausible mechanism for this suppression (Johnson et al. 2008; Dijkstra et al. 2008; Valiante et al. 2016, 2018; Trinca et al. 2022).

Pristine atomic-cooling haloes exposed to FUV radiation are also promising sites for supermassive star (SMS) formation (e.g., Inayoshi et al. 2020). In the standard picture, gas evolution and star formation in these haloes depend strongly on the external FUV intensity. Under relatively weak FUV irradiation, self-shielding during collapse allows H_2 cooling to become effective, leading to conventional Pop III star formation. Under an extremely strong FUV field with $J_{21} > J_{\rm crit} \sim 10^3$, H_2 cooling is suppressed and the gas contracts through atomic cooling at $T \simeq 8000$ K (Omukai 2001; Shang et al. 2010; Sugimura et al. 2014). [1]

The abundance of such SMS formation sites is crucial for understanding the origin of SMBHs. SMSs are expected to undergo direct collapse and leave heavy seed BHs with masses of $\sim 10^4$–$10^5\ M_\odot$, providing massive seeds for subsequent SMBH growth (Bromm &

★ E-mail: kiyuna@astr.tohoku.ac.jp

[1] Here, J_{21} denotes the FUV specific intensity at $h\nu = 12.4$ eV, the midpoint of the Lyman–Werner (LW) band, in units of 10^{-21} erg s^{-1} cm^{-2} Hz^{-1} sr^{-1}.

© 2026 The Authors

Loeb 2003; Inayoshi et al. 2020; Regan & Volonteri 2024). Sensitive near- and mid-infrared observations with JWST have identified AGN candidates out to $z \sim 7$–10 (Fan et al. 2023; Maiolino et al. 2024a,c). At $z \sim 5$, JWST has also revealed a large population of compact objects with broad-line emission, known as Little Red Dots (LRDs) (Onoue et al. 2023; Matthee et al. 2024; Greene et al. 2024; Kokorev et al. 2024; Akins et al. 2025). Although the nature of LRDs remains debated, if they host accreting BHs, their abundance is orders of magnitude higher than expected from conventional luminous-quasar luminosity functions. This may require a mechanism capable of producing heavy BH seeds relatively frequently in the early Universe.

The conventional DCBH formation scenario, however, requires a pristine atomic-cooling halo to be exposed to an extremely strong external FUV field with $J_{21} > J_{\rm crit}$ (Bromm & Loeb 2003; Visbal et al. 2014; Regan et al. 2017). Such strong irradiation is often accompanied by metal enrichment from the same nearby sources, making haloes that simultaneously satisfy the requirements of intense FUV irradiation and pristine gas relatively rare. The predicted DCBH number density may therefore be too small to account for the entire SMBH population (Dijkstra et al. 2008; Habouzit et al. 2016; Chon et al. 2016).

Recently, Chon & Omukai (2025) showed that SMSs with $\gtrsim 10^5$ $M_\odot$ can form even in slightly metal-enriched gas, provided that $Z \lesssim 10^{-3} Z_\odot$. This relaxes the requirement of pristine gas and substantially broadens the environments in which heavy BH seeds may form. However, their calculations assume an environment exposed to an extremely strong external FUV radiation field with $J_{21} > J_{\rm crit}$. It is therefore important to determine whether this remaining environmental requirement can also be relaxed, allowing SMS formation under the more common condition $J_{21} < J_{\rm crit}$.

SMS formation is generally considered difficult under subcritical FUV irradiation, $J_{21} < J_{\rm crit}$. As the gas density and column density increase during collapse, self-shielding suppresses H_2 photodissociation and allows H_2 cooling to become effective. The resulting rapid temperature decrease promotes fragmentation, preventing the nearly monolithic collapse characteristic of the supercritical regime, $J_{21} > J_{\rm crit}$. Previous numerical simulations have indeed shown that very massive Pop III stars can form under such conditions, but their masses typically remain $\lesssim 10^4$ $M_\odot$ (Regan et al. 2020; Latif et al. 2021).

Rapid halo growth can dynamically heat the gas and suppress H_2 cooling and star formation, allowing the halo to reach the atomic-cooling scale and form an SMS even under subcritical FUV irradiation (Wise et al. 2019). This pathway, however, requires H_2 cooling and the resulting star formation to be suppressed before SMS formation begins. Whether a system can instead transition to SMS formation after H_2 cooling has already triggered star formation under subcritical FUV irradiation has remained unclear.

Previous simulations of atomic-cooling haloes under subcritical FUV irradiation have mainly emphasized the initial star-formation episode triggered by H_2 cooling and the subsequent growth of the resulting massive stars (Regan et al. 2020; Latif et al. 2021). Massive Pop III stars formed during this early phase themselves become strong sources of FUV and ionizing radiation, substantially altering the radiative environment within the halo. Their FUV radiation can photodissociate H_2 in the surrounding gas, suppressing H_2 cooling and further fragmentation and potentially allowing the warm gas reservoir to undergo large-scale collapse. The initial star formation may therefore itself create the conditions for subsequent SMS formation.

The impact of radiation from stars formed earlier in the same halo on subsequent gas collapse has been explored in several studies. Dunn et al. (2018) and Chiaki et al. (2023) suggested that FUV radiation from stars formed earlier in the same halo can suppress H_2 cooling and create conditions favourable for SMS formation. More recently, Sullivan et al. (2025) found that FUV radiation from stars formed through H_2 cooling suppresses H_2 cooling and accretion in nearby collapsing clumps, although their calculations did not lead to SMS formation. These studies demonstrate that radiation from an earlier generation of stars can strongly modify subsequent gas collapse, but the longer-term response of the surrounding halo-scale gas reservoir remains unclear. In particular, no previous study has self-consistently followed the evolution from the initial star formation triggered by H_2 cooling through the subsequent halo-scale collapse to determine whether SMSs actually form and what stellar system emerges.

In this study, we perform cosmological radiation-hydrodynamic simulations of star formation in pristine atomic-cooling haloes exposed to subcritical FUV backgrounds with $J_{21} \lesssim 10^2$, following their evolution for $\sim$ 1–2 Myr after the onset of star formation. We include both FUV and ionizing radiation from Pop III stars formed within the halo and follow how their radiative feedback affects the subsequent halo-scale gas evolution and star formation.

We find that star formation proceeds through a characteristic two-stage evolution. Once self-shielding allows H_2 cooling to become effective, the gas fragments and Pop III stars form in the resulting dense cores. Internal FUV radiation from these stars subsequently photodissociates H_2 and suppresses further fragmentation, while the surrounding atomic-cooling gas reservoir continues to contract under self-gravity and eventually undergoes global collapse. This global collapse produces rapidly accreting SMSs in the central region, surrounded by a compact, strongly top-heavy Pop III stellar system. This mechanism substantially relaxes the external FUV intensity required for SMS and heavy BH seed formation, suggesting that heavy seeds may form in a wider range of environments than previously considered.

The remainder of this paper is organized as follows. In Section 2, we describe the numerical framework and simulation setup. In Section 3, we present the star formation and gas evolution within the atomic-cooling halo. In Section 4, we discuss heavy seed BH formation and subsequent growth, cosmological abundance, and observational comparisons with Pop III galaxy candidates and LRDs. Finally, we summarize our conclusions in Section 5. Throughout this paper, we adopt the cosmological parameters of Planck Collaboration et al. (2014).

2 METHODS

2.1 Numerical Framework

We perform radiation-hydrodynamic simulations of star formation in an atomic-cooling halo using the N-body + SPH code GADGET-3. The simulations follow the coupled evolution of dark matter and gas under gravity and hydrodynamics, together with radiative feedback from newly formed stars. The basic numerical implementation follows Chon & Omukai (2025).

2.2 Initial Conditions and Simulation Setup

The comoving box size is 20 h^{-1} Mpc, and we target an atomic-cooling halo previously identified as a DCBH formation site by Chon et al. (2016). The halo has a spin parameter of $\lambda \simeq 0.05$ (Chon et al. 2016), which is typical of the lognormal distribution of halo spin parameters (Bullock et al. 2001). We fix the metallicity at $Z = 10^{-6}$ $Z_\odot$.

Metal-line cooling is negligible at this metallicity, so thermal evolution is essentially identical to that of primordial gas (Omukai et al. 2008).

Previous simulations of this halo adopted a much stronger external FUV field, $J_{21} \sim 10^3$ (Chon et al. 2016, 2018). Here, to examine how heavy seed BH formation depends on the external FUV intensity, we instead consider three lower FUV intensities, $J_{21} = 1,\ 10,\ 10^2$. The external radiation field is represented by a blackbody spectrum with an effective temperature of $T_{\rm eff} = 10^4$ K. We perform three independent cosmological simulations from the same initial conditions at $z = 99$, imposing a different value of J_{21} in each run, because the external FUV intensity affects the chemical, thermal, and dynamical evolution of the gas. In all runs, the onset of star formation occurs at approximately $z \simeq 13$, when the halo mass and virial radius are $M_{\rm halo} \simeq 1.5 \times 10^8$ M$_\odot$ and $r_{\rm vir} \simeq 0.9$ kpc, respectively.

In the cosmological simulations, gas particles are retained within a physical radius of 1 kpc around the halo, while dark-matter particles are distributed over a larger region. When the maximum gas density reaches $n_{\rm H} > 10^{10}$ cm^{-3}, shortly before the onset of star formation, we extract a snapshot and cut out the region within 500 pc of the halo centre. We use this region as the initial condition for the subsequent non-cosmological simulation, neglecting cosmic expansion.

We define $t = 0$ as the onset of star formation in the computational domain and follow the subsequent evolution for up to $t = 2$ Myr. Stars with $m_\star \gtrsim 10^2$ M$_\odot$ have characteristic lifetimes of ~ 2 Myr (Schaerer 2002), after which feedback from supernova explosions may become important. In practice, some runs are terminated before $t = 2$ Myr because long-lived dense gas structures force the timestep to become extremely short, substantially increasing the computational cost.

2.3 Chemistry, Cooling, and Radiative Transfer

We solve a primordial non-equilibrium chemical network including HI, HII, e$^-$, H_2, and H^-, and follow the thermal evolution of the gas including radiative cooling and thermal processes associated with chemical and photochemical processes. The reaction rates, cooling and heating functions, and their numerical implementation follow Chon et al. (2021) and Chon & Omukai (2025).

The radiation field consists of a uniform external FUV background and local radiation from stars formed within the computational domain. We use the radiative-transfer implementation described by Chon & Latif (2017). The radiation field is divided into two energy bins: EUV photons with $h\nu > 13.6$ eV and FUV photons with $h\nu < 13.6$ eV. For radiation from stellar sources, we account for the attenuation of the EUV and FUV fluxes during radiative transfer. The EUV opacity is due to HI bound–free absorption, while the FUV opacity includes H^- bound–free absorption, HI bound–free absorption from the $2s$ and $2p$ states, HI Rayleigh scattering, and Thomson scattering by free electrons. The attenuated radiation field is then coupled to the thermochemical network through HI photoionization, H_2 photodissociation, and H^- photodetachment. The H_2 column density is calculated along the radiation path, and H_2 self-shielding is evaluated using the fitting formula of Wolcott-Green et al. (2011).

2.4 Particle Splitting and Sink Particle Model

We employ particle splitting to resolve high-density gas collapse and represent newly formed stars with sink particles.

Particle splitting is implemented following Kitsionas & Whitworth (2002). Each SPH particle is split into 13 daughter particles whenever it crosses one of the prescribed density thresholds (see also Chon et al. 2021). In both the cosmological and non-cosmological calculations, we adopt $n_{\rm H} = 10^1,\ 10^3,\ 10^7,\ 10^9$ cm^{-3} as the splitting thresholds. The initial particle masses are 120 M$_\odot$ for dark matter and 20 M$_\odot$ for gas. After four levels of splitting, the gas particle mass reaches 7×10^{-4} M$_\odot$.

Particle splitting allows us to resolve the Jeans mass with a sufficient number of SPH particles. At the sink-formation density, the Jeans mass is:

$$M_{\rm J} \simeq 0.3\ {\rm M}_\odot \left(\frac{n_{\rm H}}{2\times10^{11}\ {\rm cm}^{-3}}\right)^{-1/2} \left(\frac{T}{10^3\ {\rm K}}\right)^{3/2}, \quad (1)$$

and is resolved by $\gtrsim 500$ SPH particles. This exceeds the ~ 80-particle criterion for resolving self-gravitating fragmentation (Bate & Burkert 1997).

Cooling is turned off for gas with $n_{\rm H} > 10^{11}$ cm^{-3}. An SPH particle is replaced by a sink particle when its density exceeds $n_{\rm H} = 2 \times 10^{11}$ cm^{-3} and it lies at a local minimum of the gravitational potential. The sink radius is set to four times the SPH smoothing length at sink formation. Estimating the smoothing length from the local Jeans scale gives a characteristic sink radius of

$$r_{\rm sink} \sim 4.5 \times 10^{-3}\ {\rm pc} \left(\frac{T}{10^4\ {\rm K}}\right)^{1/2}. \quad (2)$$

SPH particles entering the sink radius are accreted onto the sink, and their masses are added to the sink-particle mass. The sink accretion rate is evaluated by averaging the accreted mass over the dynamical timescale at the sink radius. Two sink particles are merged when their separation becomes smaller than the sum of their sink radii.

Radiative feedback is included from all stars represented by sink particles. Each star is treated as a blackbody radiation source. Its stellar radius and luminosity are determined from pre-computed protostellar-evolution tables as functions of the stellar mass and mass accretion rate, and the effective temperature is calculated from the resulting luminosity and radius. The tables are based on one-dimensional protostellar-evolution calculations and cover the normal protostar phase, including pre-main-sequence evolution, as well as the bloated supergiant-protostar configurations associated with high accretion rates (Hosokawa & Omukai 2009; Hosokawa et al. 2012). In our implementation, the stellar properties used for radiative feedback are updated based on the current stellar mass and the mass accretion rate, which is evaluated from the mass growth over a time interval comparable to the dynamical time at the sink radius. We therefore do not explicitly follow the gradual Kelvin–Helmholtz contraction and the corresponding increase in $T_{\rm eff}$ after a high-accretion episode. We have checked that calculations explicitly including this contraction show no clear quantitative differences in the results discussed here.

After particle splitting, the Jeans mass of a molecular-cooling cloud core, $M_{\rm J} \simeq 0.3$ M$_\odot$ is resolved with approximately 500 SPH particles. This comfortably satisfies the Bate & Burkert (1997) criterion of ~ 80 particles for resolving self-gravitating fragmentation.

Fragmentation below the sink scale is not resolved in our simulations. The resulting multiplicity and stellar mass distribution below $\sim$ 10–100 M$_\odot$ may therefore depend on numerical resolution. Throughout this paper, we refer to individual sink particles as stars for simplicity.

3 RESULTS

We first provide an overview of the overall evolution in Section 3.1. The detailed evolution during each stage is described in Sections 3.2–3.4, followed by the resulting stellar mass distribution in Section 3.5.

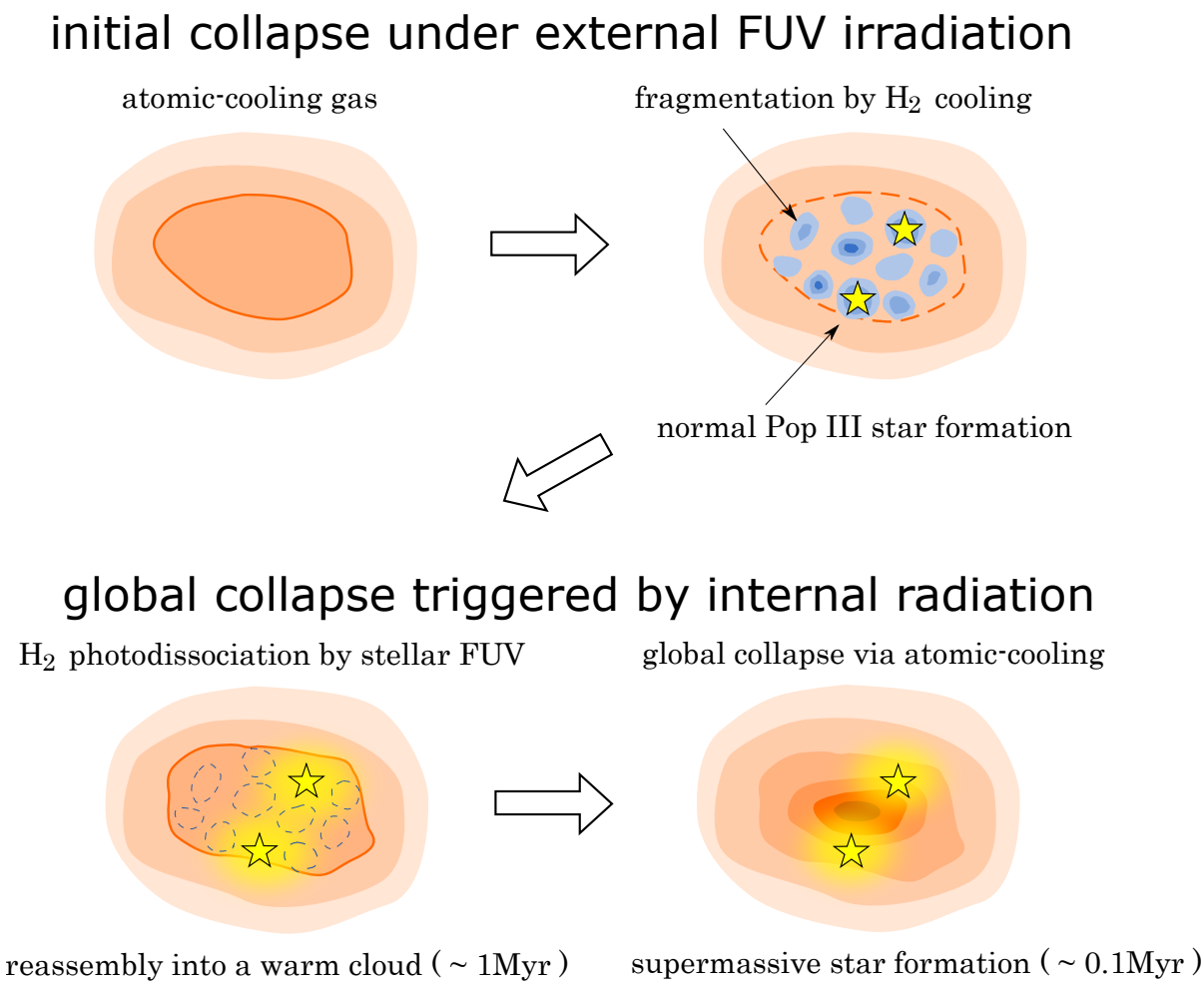


Figure 1. Schematic of the evolutionary sequence of gas collapse in the central region of an atomic-cooling halo exposed to a moderate FUV background. From left to right, the schematic depicts the initial collapse and fragmentation of the gas, the formation of normal Pop III stars, the subsequent reassembly of the fragmented gas into a larger warm clump, and the eventual global collapse triggered by internal irradiation. White arrows indicate the direction of time evolution. Orange and blue shaded regions represent warm ($T \sim 8000$ K) and H_2-cooled ($T \sim 400$ K) gas, respectively; within each region, progressively darker shading denotes increasing gas density. Yellow star symbols indicate normal Pop III stars. Dashed outlines mark the preceding spatial configurations of gas structures and are retained as visual guides to illustrate their subsequent fragmentation or reassembly.

3.1 Overview: Two modes of star formation during initial and global collapse

In all runs, star formation proceeds through a characteristic two-stage evolution. During the initial collapse, the gas cloud fragments into numerous clumps, with normal Pop III stars forming in some of them. Radiative feedback from these stars subsequently suppresses further fragmentation and promotes the reassembly of the fragmented gas into a larger warm cloud. The subsequent large-scale collapse of this reassembled cloud, which we refer to as global collapse, drives rapid star formation and the growth of SMSs. While the reassembly of the gas occurs over ~ 1 Myr, the subsequent runaway collapse from $n_{\rm H} \sim 10^5$ cm^{-3} proceeds over only ~ 0.1 Myr. Figure 1 schematically summarizes this evolutionary sequence inferred from the simulations. The thermochemical and dynamical evolution during each stage is described in detail in Sections 3.2–3.4.

Figure 2 shows the stellar mass evolution in each run. The upper panel shows the time evolution of the total stellar mass. In all runs, the initial episode of star formation is followed by a period of relatively weak star-formation activity. The total stellar mass then begins to increase rapidly around the epochs marked by the black open circles. These epochs are identified as the onset of star formation induced by the global collapse, as examined in detail in Section 3.4, and mark the transition to the subsequent SMS formation phase. The increase is more gradual in the $J_{21} = 10$ run, where substantial star formation already occurs before the global collapse.

Star formation associated with the global collapse begins at $t = 0.86$ Myr for $J_{21} = 10^2$, $t = 0.73$ Myr for $J_{21} = 10$, and $t = 1.95$ Myr for $J_{21} = 1$. By the end of each simulation, the most massive star has grown to more than 10^4 M$_\odot$ and contains approximately 20–40 % of the total stellar mass (see the bottom panel of Figure 2). Thus, a substantial fraction of the stellar mass formed during the global-collapse phase is concentrated in the most massive star. We terminated the simulations at $t = 1$ Myr for the $J_{21} = 10^2$ and 10 runs and at $t = 2$ Myr for the $J_{21} = 1$ run because the increasingly short timesteps made further evolution computationally expensive.

Figure 3 shows the mass evolution and mass-accretion rates of individual star particles. The upper panel shows that stars formed during

Table 1. Summary of the simulations and resulting stellar properties. For each run, we list the external FUV intensity, the epoch of the global collapse, the simulation end time, the total stellar mass at the final snapshot, and the mass of the most massive star particle.

Run	J_{21}	$t_{\rm gc}$ [Myr]	$t_{\rm end}$ [Myr]	$M_{\star,\rm tot}$ [$M_\odot$]	$m_{\star,\rm max}$ [$M_\odot$]
J1e2	10^2	0.86	1	1.8×10^5	5.8×10^4
J1e1	10	0.73	1	1.3×10^5	2.2×10^4
J1e0	1	1.95	2	7.1×10^4	2.3×10^4

the early phase generally cease growing at $m_\star \lesssim 10^2$–10^3 $M_\odot$, although a few reach masses above 10^3 $M_\odot$. In contrast, a small number of stars newly formed during the global-collapse phase undergo sustained mass accretion and grow into SMSs. Numerous lower-mass stars are also formed during this phase. Thus, SMS formation in our simulations occurs together with the formation of a surrounding stellar cluster.

The total stellar mass and the mass of the most massive star at the end of each simulation are summarized in Table 1. For example, in the $J_{21} = 10^2$ run, the total stellar mass reaches $\sim 1.8\times10^5$ $M_\odot$, while the most massive star grows to $\sim 5.8\times10^4$ $M_\odot$. The lower panel of Figure 3 shows that the most massive stars maintain high accretion rates of $\dot{m}_\star \sim 10^{-1}$ $M_\odot$ yr^{-1}, which, if sustained, would allow them to grow into SMSs with $m_\star \sim 10^5$ $M_\odot$ on a timescale of ~ 1 Myr.

The high accretion rates onto the most massive stars persist until the end of the simulations, suggesting that these stars may continue to grow substantially beyond the masses reached in the present calculations. This further growth may be affected by supernova explosions from the earlier stellar population, which could modify the subsequent gas supply. We discuss this uncertainty in Section 4.1.

Although the three runs differ in their detailed time evolution and degree of fragmentation, they share the same broad evolutionary sequence: the formation of normal Pop III stars during the initial collapse, the reassembly of the fragmented gas into a larger warm cloud, and the subsequent formation of SMSs during the global collapse.

3.2 Initial Collapse: Pop III Star Formation via H_2 Cooling

We first examine star formation during the initial collapse. Figure 4 shows the gas temperature and H_2 fraction as functions of density just before the formation of the first protostar in the three runs. The temperature and H_2 fraction are evaluated as mass-weighted mean values in each density bin. For all external FUV intensities considered, the gas temperature drops sharply from $\sim 10^4$ K, characteristic of atomic cooling, at $n_{\rm H} \sim 10^2$–10^4 cm^{-3}. As the central gas becomes denser, H_2 self-shielding against the external FUV radiation becomes effective, allowing the H_2 fraction to increase and H_2 cooling to lower the gas temperature. This transition shifts to higher densities with increasing external FUV intensity. The H_2 fraction saturates at $\sim 10^{-3}$, as expected for H_2 formation through the H^- channel. The subsequent thermal evolution follows the standard H_2-cooling track of primordial star formation (Omukai 2000, 2001). The transition from the initial atomic-cooling track to the molecular-cooling track is consistent with previous studies of primordial collapse under sub-critical external FUV fields with $J_{21} < J_{\rm crit}$ (e.g. Shang et al. 2010; Sugimura et al. 2014).

Figure 5 shows the gas structure within the central few tens of parsecs for the $J_{21} = 10^2$ run. At the onset of initial star formation,

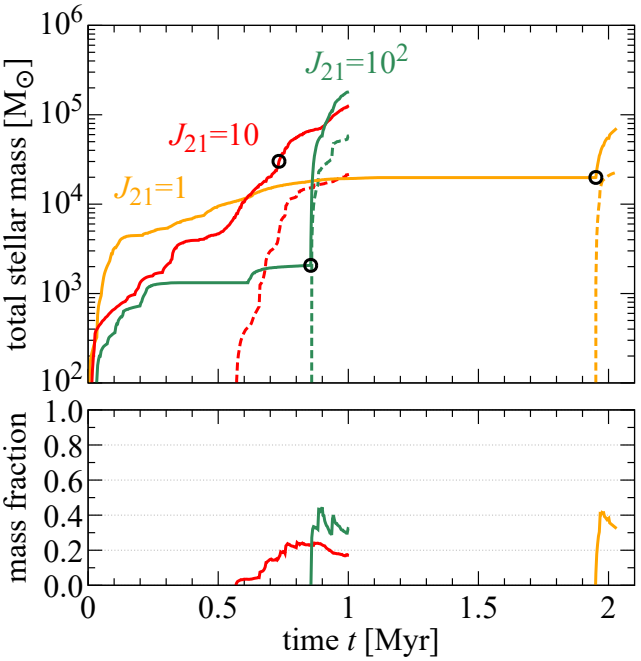


Figure 2. Time evolution of stellar masses in the atomic-cooling halo in the three runs. The horizontal axis shows the elapsed time since the onset of the initial star formation, t. Hereafter, the "most massive star" refers to the star particle that is the most massive at the end of each simulation. *Top panel:* Evolution of the total stellar mass (solid lines) and the mass of the most massive star (dashed lines). The green, red, and orange lines correspond to the runs with $J_{21} = 10^2$, 10, and 1, respectively. Black open circles mark the onset of star formation associated with the global collapse (see text for definition). *Bottom panel:* Fraction of the total stellar mass contained in the most massive star.

a gas structure with a characteristic density of $\sim 10^3$ cm^{-3} extends over the central ~ 10 pc region and contains numerous dense cores reaching $\gtrsim 10^4$ cm^{-3}. These dense cores have lower temperatures and higher H_2 fractions than the surrounding gas, with H_2 abundances sufficiently high for efficient H_2 cooling. The individual cores have characteristic sizes of ~ 1 pc, and approximately 10^2 such cores are distributed throughout the ~ 10 pc region.

This fragmentation is triggered by the rapid temperature decrease associated with the onset of H_2 cooling, which reduces thermal pressure support against self-gravity. The characteristic densities at which the cores form, $n_{\rm H} \sim 10^{4-5}$ cm^{-3}, approximately coincide with those at which the temperature drops owing to H_2 cooling in Figure 4. For a dense core with $n_{\rm H} \sim 10^4$ cm^{-3} and $T \sim 4\times10^2$ K, the Jeans length is

$$\lambda_{\rm J} \sim 1\ {\rm pc}\left(\frac{n_{\rm H}}{10^4\ {\rm cm^{-3}}}\right)^{-1/2}\left(\frac{T}{4\times10^2\ {\rm K}}\right)^{1/2}, \quad (3)$$

which is comparable to the sizes of the individual cores seen in Figure 5. On a larger scale, the overall ~ 10 pc extent of the core distribution is comparable to the Jeans length of the surrounding warm gas with $n_{\rm H} \sim 10^3$ cm^{-3} and $T \sim 8\times10^3$ K. The ratio of the Jeans mass of this warm atomic gas to that of the H_2-cooled gas is

$$\frac{M_{\rm J}(10^3\ {\rm cm^{-3}}, 8\times10^3\ {\rm K})}{M_{\rm J}(10^4\ {\rm cm^{-3}}, 4\times10^2\ {\rm K})} \sim 10^2. \quad (4)$$

Interestingly, this ratio is of the same order as the number of dense cores present at the onset of initial star formation in Figure 5. The initial cloud structure can therefore be interpreted as a self-gravitating warm gas structure on a scale of ~ 10 pc that fragments through H_2 cooling into numerous pc-scale cores. Similar fragmentation is also

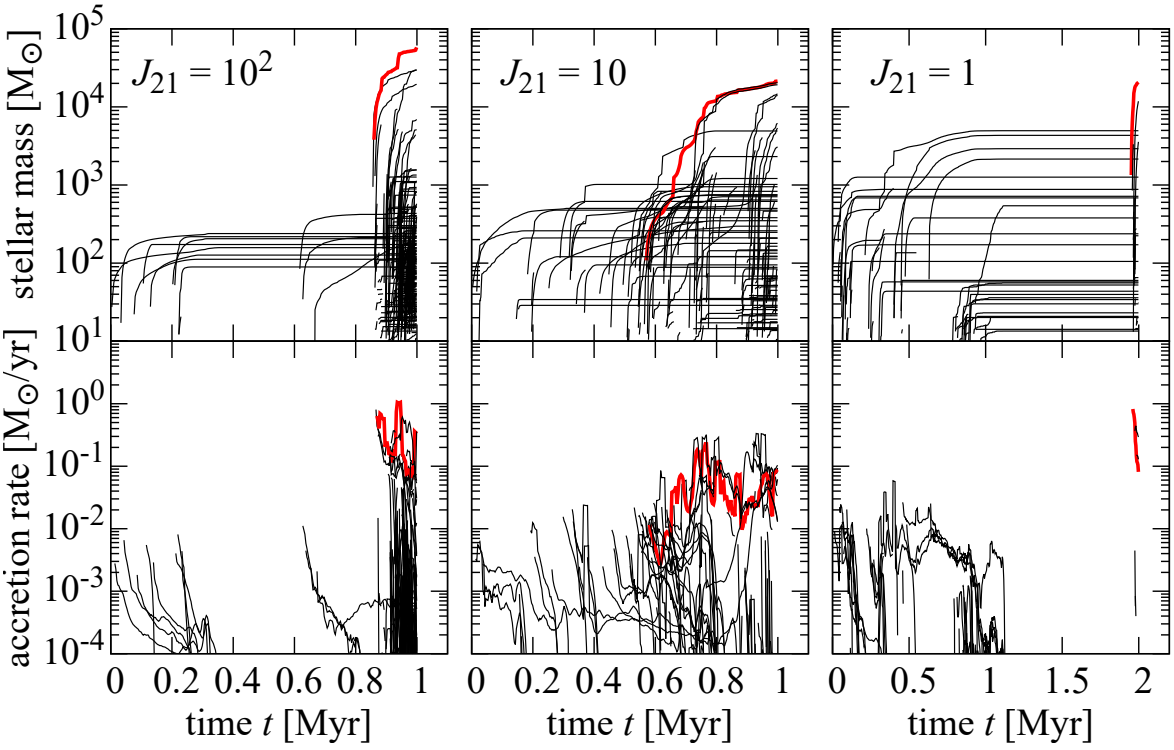


Figure 3. Time evolution of individual stellar masses and their accretion rates in the atomic-cooling halo for the three runs. The horizontal axis shows the elapsed time since the onset of the initial star formation, t, while the vertical axis represents either the stellar mass or the mass-accretion rate. *Top panels:* Mass evolution of individual stars. Black lines show all star particles, while the red line highlights the star particle that becomes the most massive by the end of each simulation. From left to right, the panels correspond to the runs with $J_{21} = 10^2$, 10, and 1. *Bottom panels:* Time evolution of the mass-accretion rates of individual stars. Black lines show all star particles, while the red line highlights the same star particle as in the corresponding top panel.

seen in the $J_{21} = 10$ and 1 runs shown in Figures 6 and 7, although the detailed morphology differs among the runs. Note that $J_{21} = 10^2$ maps use a smaller field of view than those for the $J_{21} = 10$ and 1 runs to better show the more spatially confined fragmenting region.

We next estimate how the characteristic fragmentation mass varies with the external FUV intensity. The characteristic mass scale can be estimated from the Jeans mass at the temperature minimum in Figure 4. A stronger external FUV field requires a larger column density for effective H_2 self-shielding, shifting the onset of the temperature decline and the subsequent temperature minimum to higher densities. Accordingly, the characteristic Jeans mass increases toward weaker external FUV fields, from $\sim 6{\times}10^2$ M$_\odot$ for $J_{21} = 10^2$ to $\sim 2{\times}10^3$ M$_\odot$ for $J_{21} = 1$. The relation between this fragmentation mass scale and the stellar mass distribution that subsequently develops is discussed in Section 3.5.

3.3 Suppression of Fragmentation by Internal Radiative Feedback

After the onset of star formation, radiative feedback from the newly formed stars rapidly alters the small-scale gas structure. The pc-scale H_2-cooled clumps formed during the initial collapse gradually disappear, while further small-scale fragmentation and star formation are strongly suppressed. At the same time, the larger self-gravitating gas structure is not dispersed, but instead reassembles into a warmer and more coherent cloud. As shown in the following section, this reassembled warm cloud subsequently undergoes global collapse.

At the onset of star formation, $\sim 10^2$ dense cores produced by H_2 cooling are distributed within a larger, self-gravitating gas structure extending over $\sim$ 10 pc. In the $J_{21} = 10^2$ run, however, only seven stars have formed by $t = 0.5$ Myr. Thus, most of the dense cores produced during the initial collapse do not subsequently proceed to star formation. Radiative feedback from the newly formed stars, through photodissociation, reduces the H_2 fraction in the central region. Consequently, the low-temperature, H_2-rich clumpy structure present at the onset of star formation largely disappears by $t = 0.5$ Myr. In contrast, the larger central gas structure on a scale of $\sim$ 10 pc remains largely intact. As the embedded pc-scale clumpy structure is erased, the gas reassembles into a larger warm cloud.

The gas that has cooled and condensed through H_2 cooling is subsequently irradiated by the newly formed stars. As H_2 is photodissociated, further molecular cooling is suppressed, and compressional heating raises the gas temperature to $T \sim 8 \times 10^3$ K. At $t = 0.5$ Myr in Figure 5, the gas has reassembled into a larger dense structure with $n_H \sim 10^4$ cm^{-3}, extending over $\sim$ 5–10 pc. This scale is broadly consistent with the Jeans length, $\lambda_J \sim 5$ pc, for gas with $n_H \sim 10^4$ cm^{-3} and $T \sim 8 \times 10^3$ K. By suppressing H_2 cooling and thereby raising the gas temperature, internal radiative feedback thus increases the characteristic Jeans scale from $\sim$ 1 pc to $\sim$ 5 pc, suppressing further small-scale fragmentation. FUV feedback from Pop II stars in low-metallicity galaxies has similarly been found to suppress H_2 cooling and small-scale fragmentation, promoting the formation of a more massive warm gas structure (Sugimura et al. 2024).

We next estimate the FUV intensity produced by the newly formed stars to assess whether it is sufficient to suppress H_2 cooling in the central region. For a total stellar mass of $\sim 10^3$ M$_\odot$ during the early phase (Figures 2 and 3), the total UV luminosity is estimated to be $L_{UV} \simeq 5 \times 10^{40}$ erg s^{-1}, assuming massive Pop III stars with

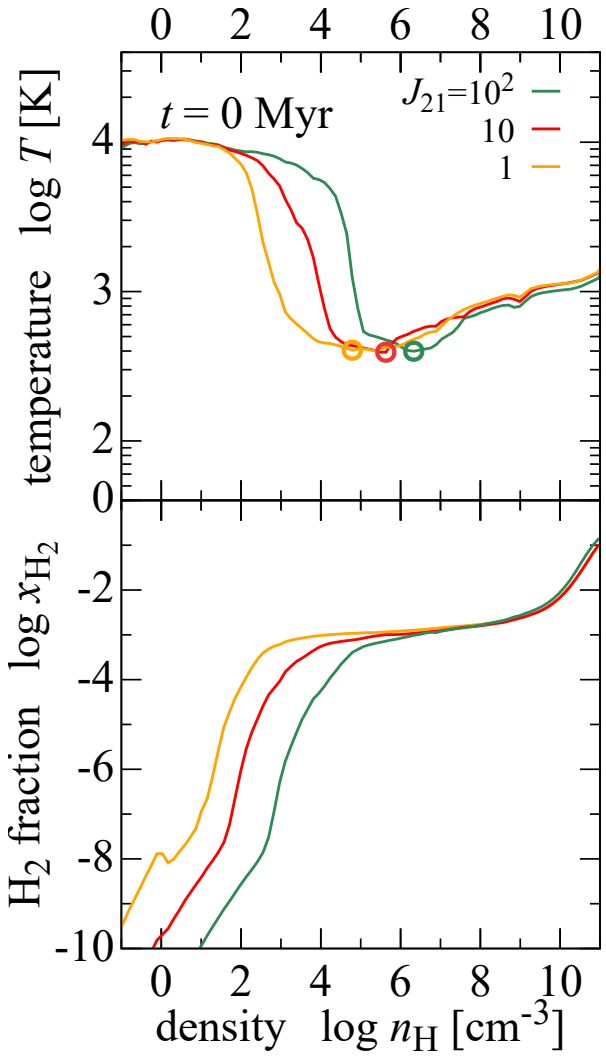


Figure 4. Temperature (top) and H_2 fraction (bottom) as functions of density just before the formation of the first protostar in the atomic-cooling halo for the three runs. The plotted values are mass-weighted averages over gas particles in each density bin. The green, red, and orange lines correspond to the runs with $J_{21} = 10^2$, 10, and 1, respectively. Black open circles in the top panel mark the temperature minimum along each curve.

$T_{\rm eff} \simeq 10^5$ K (Schaerer 2002). The corresponding local LW intensity at a distance r is

$$J_{21} \sim 10^5 \left(\frac{r}{10\ {\rm pc}}\right)^{-2}. \quad (5)$$

This exceeds the critical intensity required to suppress H_2 cooling for a hard Pop III spectrum, $J_{\rm crit}(T_{\rm eff} = 10^5\ {\rm K}) \sim 10^{4-5}$ (Shang et al. 2010; Sugimura et al. 2014). The resulting internal radiation field can therefore suppress H_2 cooling, and hence the associated fragmentation, throughout the central ~ 10 pc region.

We note that the critical intensity $J_{\rm crit}$ is conventionally defined for externally irradiated collapsing clouds, using either one-zone models or three-dimensional simulations with an imposed radiation field. The present case differs in that the radiation sources form within the cloud, and the irradiation varies in both space and time after fragmentation has already begun. Thus, $J_{\rm crit}$ should not be regarded as a sharp quantitative threshold for the present system. Nevertheless, the estimated stellar FUV intensity exceeds the conventional $J_{\rm crit}$, consistent with the strong suppression of H_2 cooling and further fragmentation seen in our simulations.

3.4 Transition to Atomic Cooling and Global Collapse

From $t = 0.5$ Myr to 0.86 Myr in Figure 5, the pc-scale clumpy structure progressively disappears, while the gas is reassembled into a single, larger cloud on a scale of several parsecs. This reassembled cloud consists predominantly of warm gas in which H_2 has been photodissociated by radiation from stars formed within the cloud, and continues to contract under atomic cooling and self-gravity.

Figure 8 shows the temperature and H_2 fraction as functions of density during this phase for the different external FUV intensities. In contrast to the initial-collapse phase shown in Figure 4, where dense cores are cooled to a few hundred K by H_2 cooling, most of the dense gas with $n_{\rm H} \gtrsim 10^6$ cm^{-3} now lies along the atomic-cooling track at $T \sim 8000$ K. The H_2 fraction remains at only $\sim 10^{-7}$, well below the characteristic value $x_{\rm H_2} \sim 10^{-4}$ above which H_2 cooling becomes important (Yoshida et al. 2003). Thus, as a consequence of the suppression of H_2 cooling by internal radiative feedback, the global collapse proceeds along the atomic-cooling track rather than the molecular-cooling track.

The global collapse therefore represents a different mode of collapse from that during the initial-collapse phase. During the initial collapse, the collapsing gas fragments through H_2 cooling into numerous dense cores. During the global collapse, by contrast, the larger-scale warm cloud collapses as a whole without undergoing such small-scale fragmentation. The interval between the onset of the initial star formation and the global collapse is $t \sim 0.8$ Myr. This is comparable to the free-fall time, $t_{\rm ff} \sim 1$ Myr, of the larger-scale gas structure at $n_{\rm H} \sim 10^{3-4}$ cm^{-3}, from which the dense cores initially fragment.

All three runs eventually undergo global collapse, although the pathway leading to it varies with the external FUV intensity. In the $J_{21} = 10^2$ run discussed above, the pc-scale fragmented structure is largely erased by internal radiative feedback, while the larger-scale gas structure remains near the halo centre and is reassembled into a warm cloud. Continued gas accumulation then drives this cloud into global collapse predominantly through atomic cooling.

The $J_{21} = 10$ run follows a broadly similar evolution, but the suppression of H_2 cooling and fragmentation is less complete. A large-scale self-gravitating gas structure is already present at the onset of star formation and remains near the halo centre as gas continues to accumulate. Unlike in the $J_{21} = 10^2$ run, however, some of the dense clumps produced during the initial collapse survive until the global collapse. Figure 6 shows several such dense cores in the vicinity of the collapse centre. Figure 8 also shows that some dense gas at $n_{\rm H} \gtrsim 10^4$ cm^{-3} retains an H_2 fraction of $x_{\rm H_2} \sim 10^{-3}$, allowing H_2 cooling to remain effective locally. Accordingly, the $n_{\rm H}$–T distribution contains a molecular-cooling component in addition to the dominant atomic-cooling track. The large-scale gas structure nevertheless undergoes global collapse predominantly through atomic cooling, while H_2-cooled clumps remain locally within the cloud and continue to form stars. Despite this persistent local fragmentation, the most massive star ultimately grows to $m_\star > 10^4\ {\rm M}_\odot$. The large-scale gas inflow can therefore feed a small number of rapidly growing stars even in the presence of local fragmentation, reminiscent of the supercompetitive accretion process discussed by Chon & Omukai (2020).

In the $J_{21} = 1$ run, the pathway to global collapse differs more substantially. Radiative feedback from a massive star formed during the initial collapse drives the expansion of a large ionized bubble

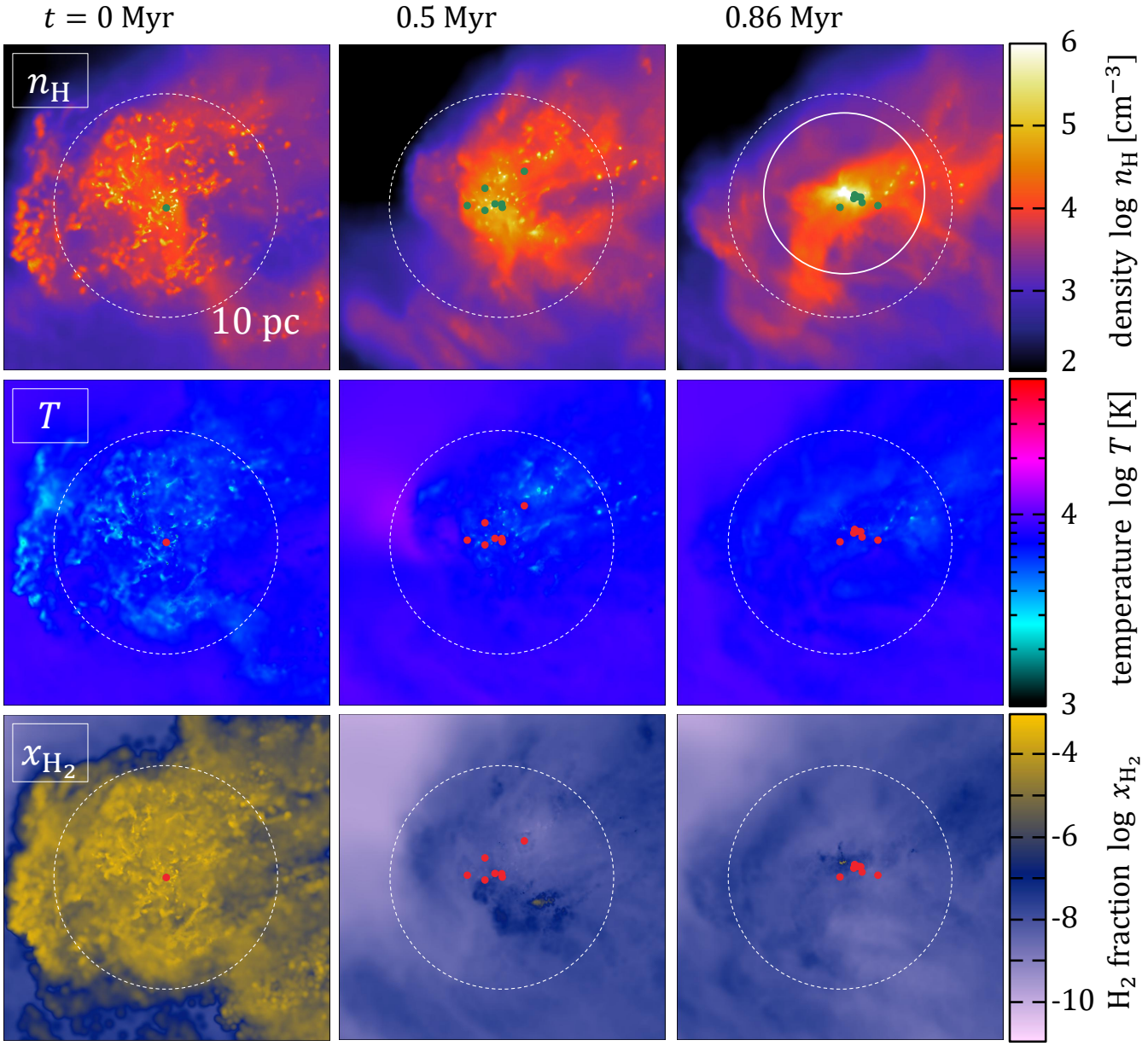


Figure 5. Mass-weighted projected maps of gas properties in the $J_{21} = 10^2$ run. From left to right, the panels correspond to $t = 0$, 0.5, and 0.86 Myr after the onset of the initial star formation in the halo. Each panel is centred on the first-formed star particle. The three rows show density (top), temperature (middle), and H_2 fraction (bottom). Green or red points indicate star particles. Dashed white circles mark a radius of 10 pc from the centre. In the top-right panel, the white solid circle indicates the region undergoing global collapse. Its radius is 7.2 pc, corresponding to the collapse radius estimated from the minimum in the r–$\dot{M}$ diagram (Figure 9), and broadly comparable to the Jeans length of the warm gas cloud.

(Figure 7). Gas near the halo centre is swept outwards and accumulates at a distance of $\sim$ 30 pc ($\sim 0.03\, r_{\rm vir}$). The accumulated gas forms a neutral cloud of size $\sim$ 10 pc near the edge of the ionized region, which subsequently undergoes global collapse. Thus, unlike in the higher-J_{21} runs, global collapse occurs in a newly assembled cloud offset from the halo centre.

Although the external FUV intensity systematically affects the overall evolution, the detailed fragmentation pattern and locations of individual star-forming clumps should not be interpreted as deterministic consequences of J_{21}. These small-scale features also depend on the stochastic evolution of fragmentation and the geometry of stellar radiative feedback.

To examine how the global collapse proceeds, Figure 9 shows the radial profiles of gas density, temperature, and mass inflow rate at three epochs for each external FUV intensity. We first consider the density profiles. The dashed curves show the mass-weighted mean density within each radial bin, whereas the solid curves show the mean density enclosed within each radius,

$$\bar{n}_{\rm H} = \frac{3M_{\rm gas}(< r)}{4\pi r^3 \mu m_{\rm H}}, \tag{6}$$

where $\mu = 1.2$ is the mean molecular weight and $m_{\rm H}$ is the hydrogen mass.

The mass-weighted density profiles are sensitive to local dense clumps and therefore retain a strong signature of the fragmented structure. Several density peaks are present around $r \sim 10$ pc, cor-

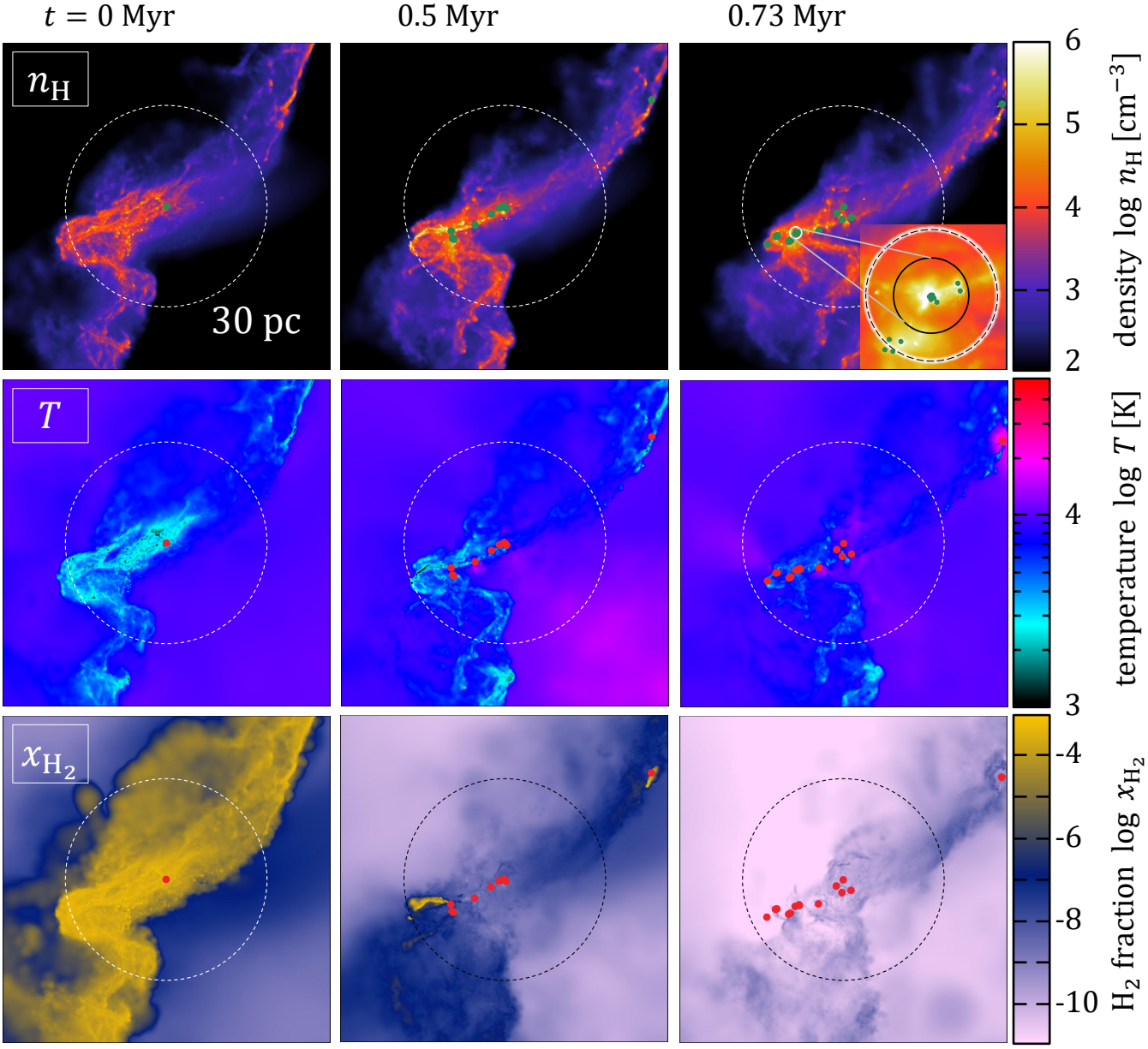


Figure 6. Same as Figure 5, but for the $J_{21} = 10$ run. From left to right, the panels correspond to $t = 0$, 0.5, and 0.73 Myr after the onset of star formation. The inset in the top-right panel shows a zoomed-in view of the region undergoing global collapse, which is marked by the solid black circle with a radius of 1.7 pc.

responding to dense clumps with $n_H \sim 10^4$ cm^{-3}. This density is consistent with the characteristic density at which H_2 cooling induces the rapid temperature decline and fragmentation during the initial collapse, as discussed in Section 3.2. By contrast, the enclosed mean density profiles average over the local clumpy structure and trace the underlying large-scale gas distribution.

At each epoch, the enclosed mean density profile consists of an approximately uniform-density central core surrounded by an envelope with $n_H \propto r^{-2}$. As the collapse proceeds, the central core contracts to progressively smaller radii, while the r^{-2} envelope extends further inwards. This evolution is characteristic of the self-similar runaway collapse of an isothermal gas (Larson 1969; Penston 1969), in which the characteristic size of the central core is approximately given by the Jeans length corresponding to the core density and temperature at each epoch.

The temperature profiles show that the collapse remains nearly isothermal at $T \simeq 5$–7×10^3 K, as regulated by atomic cooling, despite an increase in density of approximately ten orders of magnitude. The mass inflow rate rises steeply with radius within the central core and remains approximately constant at ~ 1 M$_\odot$ yr^{-1} throughout the outer envelope. This behaviour is consistent with the self-similar runaway collapse of an isothermal gas.

The characteristic inflow rate during such a collapse can be expressed as

$$\dot{M} = \phi \frac{c_s^3}{G} \simeq 1.1\ \mathrm{M_\odot\ yr^{-1}} \left(\frac{\phi}{10}\right) \left(\frac{T}{5\times10^3\ \mathrm{K}}\right)^{3/2}. \quad (7)$$

Here, ϕ is a dimensionless factor that depends on the dynamical state of the collapsing cloud. The Larson–Penston solution gives $\phi = 46.9$, corresponding to a highly dynamical collapse, whereas

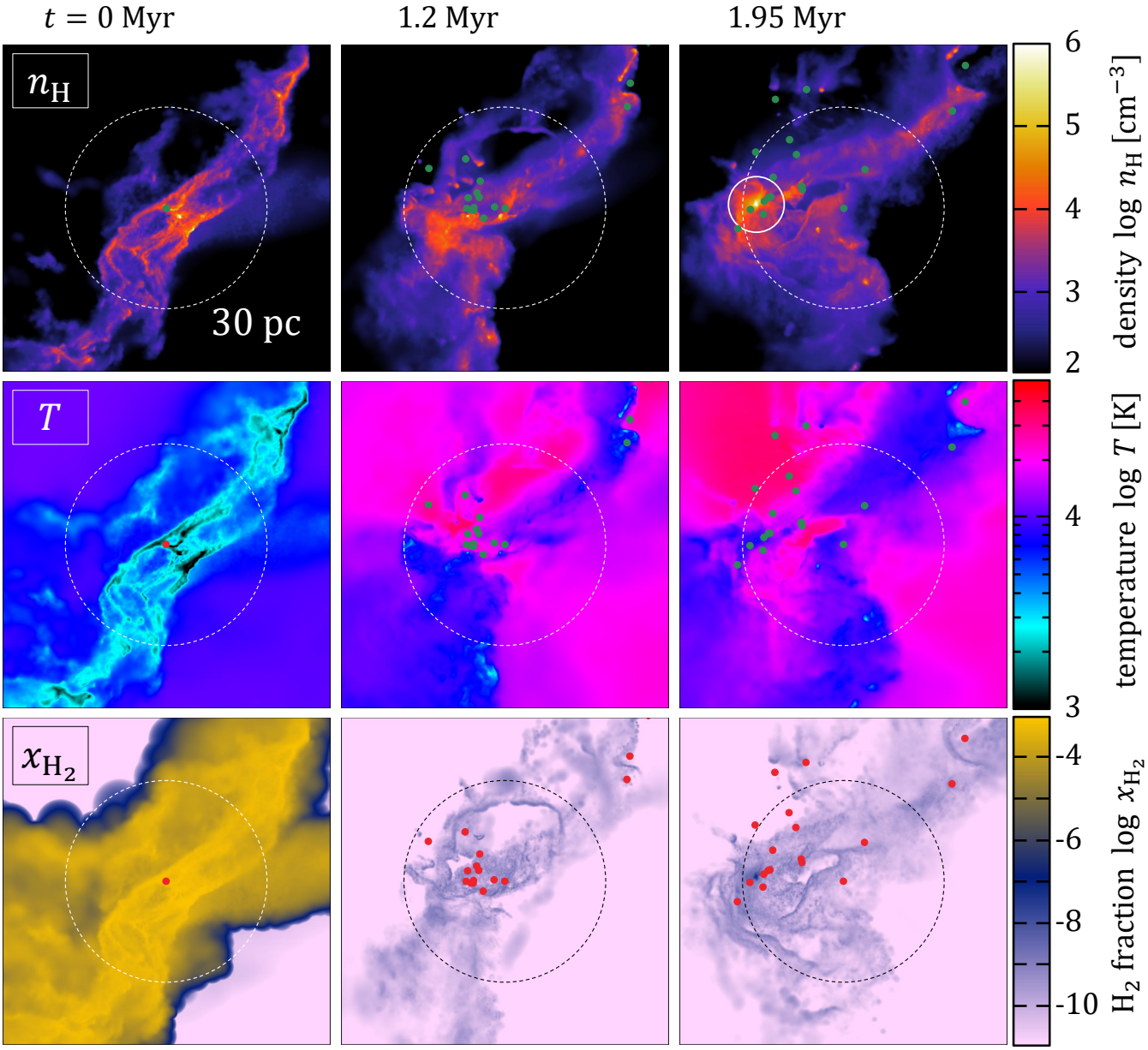


Figure 7. Same as Figure 5, but for the $J_{21} = 1$ run. From left to right, the panels correspond to $t = 0$, 1.2, and 1.95 Myr after the onset of star formation. Dashed white or black circles mark a radius of 30 pc from the centre. The solid white circle mark the region that undergoes global collapse, with a radius of 8.2 pc.

calculations starting from more realistic initial conditions typically yield $\phi \sim 10$ (Foster & Chevalier 1993). The resulting inflow rate of order 1 $M_\odot$ yr^{-1} is therefore in good agreement with that found in the simulations. The inflow-rate profile in the envelope also exhibits a local minimum around $r \sim 7$ pc. We use this minimum as an approximate measure of the fragmentation scale: inward mass transport from larger radii is partly redistributed among multiple collapsing cores rather than continuing coherently toward a single centre. The resulting scale is consistent with the extent of the fragmented region seen directly in the two-dimensional density distribution in Figure 5.

Despite substantial internal fragmentation, the global collapse therefore exhibits a clear Larson–Penston-type structure. It is not simply an ensemble of independently collapsing local clumps, but instead represents the collapse of the larger underlying gas structure as a whole.

To determine the spatial extent of the gravitationally unstable region during the global collapse, we compare the enclosed gas mass with the Bonnor–Ebert mass. Figure 10 shows the enclosed gas mass profiles immediately before the onset of star formation during the global collapse. We separately evaluate the enclosed masses of the cold gas ($T < 2\times10^4$ K) and the hot, photoionized gas ($T > 2\times10^4$ K); (see also Figure 8). The mass budget is dominated by the cold gas throughout nearly the entire collapsing region. The dashed curves show the Bonnor–Ebert mass evaluated using the properties of the cold gas, since this is the component relevant to gravitational collapse and star formation. The hot photoionized gas is excluded from this estimate because it does not directly participate in the collapse. Moreover, owing to the strong temperature dependence

$$M_{\rm BE} \propto n_{\rm H}^{-1/2} T^{3/2}, \tag{8}$$

even a small amount of hot gas can substantially raise the average temperature and lead to an overestimate of the Bonnor–Ebert mass.

The enclosed mass profiles show that, in all runs, the enclosed gas mass exceeds the Bonnor–Ebert mass over a broad radial range, indicating large-scale gravitational instability during the global collapse. For example, in the $J_{21} = 10^2$ run, this condition is satisfied over $r \sim 10^{-3}$–10^2 pc. This demonstrates that the global collapse involves gravitational instability of the large-scale gas structure, rather than only the collapse of individual dense cores produced by fragmentation. The gravitationally unstable region extends to $r \sim 10^2$ pc and contains $\simeq 5 \times 10^6$ $M_\odot$ of gas, providing an approximate upper limit to the gas mass available for star formation during this phase.

The positions and masses of stars already formed by this epoch are also shown in Figure 10. These stars are distributed over the radial range where small-scale H_2-cooled dense cores were produced by fragmentation during the initial collapse, as discussed in Section 3.2.

3.5 Stellar Mass Distribution

We now examine the stellar mass distribution, with particular emphasis on the preferential growth of massive stars following the onset of star formation induced by the global collapse. Figure 11 shows the stellar mass distributions resulting from the initial fragmentation phase (top row) and at the end of the simulations (bottom row).

We first consider the distributions produced during the initial fragmentation phase. Immediately before star formation associated with the global collapse, the number of stars already formed is somewhat larger for lower J_{21}, but remains at only $\sim$ 10–20 in all runs.

The distributions tend to extend to higher masses toward lower J_{21}, broadly consistent with the increase in the characteristic fragmentation mass estimated in Section 3.2. However, each mass bin contains at most only a few stars, so the detailed differences among the three histograms are subject to substantial stochasticity and are difficult to interpret as a systematic dependence on J_{21}.

Following the onset of star formation induced by the global collapse, the high-mass end extends substantially in all runs, with a small number of stars growing preferentially to form SMSs with masses $> 10^4$ $M_\odot$. Some of these massive stars also form gravitationally bound multiple systems. Their possible evolution into massive BH binaries is discussed in Section 4.5. Despite the development of this high-mass tail, the peak of the mass distribution remains nearly unchanged, indicating that lower-mass star formation proceeds concurrently. Star formation during the global collapse can therefore be characterized by the continued formation of lower-mass stars together with the preferential growth of a small subset into SMSs.

The final mass distributions shown in Figure 11 still show noticeable differences among the runs. The $J_{21} = 10$ and 10^2 runs both exhibit a main concentration around $\sim 10^2$ $M_\odot$ and a high-mass tail extending beyond 10^4 $M_\odot$, whereas the $J_{21} = 1$ run contains fewer intermediate-mass stars with $m_\star \sim 10^{2-3}$ $M_\odot$. The latter difference likely reflects the much shorter evolution time after the star formation induced by global collapse begins at $t \simeq 1.95$ Myr in this run. Because the number of stars in each bin is small and the apparent shape also depends on the adopted binning, however, the histograms alone are not well suited for a quantitative comparison of the mass distributions. We therefore examine the cumulative stellar mass distributions below.

We next examine how stars in different mass ranges contribute to the total stellar mass budget. We define the cumulative stellar mass contained in stars below a given mass $m_\star$ as

$$M_{\rm cum}(< m_\star) \equiv \int_0^{m_\star} m'_\star \frac{dN}{dm'_\star} dm'_\star. \tag{9}$$

Figure 12 shows this quantity normalized by the total stellar mass, $M_{\rm cum}(< m_\star)/M_{\rm tot}$. The stellar mass budget is dominated by a small number of massive stars at the high-mass end. In all runs, approximately 80–90 % of the total stellar mass is contained in stars with $m_\star > 10^3$ $M_\odot$. This behaviour is characteristic of oligarchic growth, in which the global collapse feeds a small number of massive stars.

Despite the differences visible in the binned histograms in Figure 11, the cumulative profiles at $m_\star \lesssim 10^3$ $M_\odot$ have remarkably similar shapes among the runs. All profiles rise steeply below $\sim 10^2$ $M_\odot$, reflecting the low-mass cutoff of the stellar mass distribution, and approximately follow $M_{\rm cum}(< m_\star) \propto m_\star^{2/3}$ at higher masses. This suggests that the differences in the stellar populations produced during the initial fragmentation phase do not leave a strong systematic imprint on the final mass distribution at $m_\star \lesssim 10^3$ $M_\odot$, even though they can affect the radiative-feedback history leading to the global collapse. Once the large-scale collapse becomes dominated by atomic cooling, its subsequent evolution is governed primarily by similar thermodynamics among the runs, which may account for the similarity of their stellar mass distributions. The black line in Figure 12 extends this comparison to a stronger external FUV field, showing the cumulative mass distribution reconstructed from the stellar mass function of the $J_{21} = 10^3$, $Z = 10^{-6}$ $Z_\odot$ run with radiative feedback in Chon & Omukai (2025) at $t = 2$ Myr. Its overall shape is broadly similar to those found in our simulations. This similarity suggests that, once H_2 photodissociation becomes sufficiently effective to regulate the thermal evolution of the collapsing gas, the resulting stellar mass distribution may be relatively insensitive to the precise intensity of the external FUV field.

The slope of this cumulative mass function can be related to the commonly used differential IMF slope. If the high-mass stellar mass distribution is written as

$$\frac{dN}{dm_\star} \propto m_\star^{-\alpha}, \tag{10}$$

then

$$M_{\rm cum}(< m_\star) \propto m_\star^{2-\alpha}. \tag{11}$$

Thus, the relation $M_{\rm cum}(< m_\star) \propto m_\star^{2/3}$ found in our simulations corresponds to $\alpha \simeq 4/3$. This is substantially more top-heavy than the canonical Salpeter-like high-mass slope of $\alpha \simeq 2.35$, indicating that the resulting stellar population is strongly weighted towards massive stars.

The characteristic mass scale at the low-mass end of the stellar distribution is related to the H_2-cooled fragmentation during the initial collapse. As discussed in Section 3.2, this scale is approximately set by the Jeans mass near the temperature minimum and increases toward weaker external FUV irradiation. This broadly accounts for the mass range populated by stars formed during the initial star-formation episode.

The location of this peak is also close to the numerical resolution limit of our sink treatment. For reference, the Bondi radius is $r_{\rm Bondi} \simeq 2.5 \times 10^{-3}$ pc$(m_\star/100\ M_\odot)(T/10^4\ {\rm K})^{-1}$, and becomes comparable to or larger than the adopted sink radius for $m_\star \sim 10$–10^2 $M_\odot$, depending on the gas temperature. The detailed shape and characteristic mass at the low-mass end may therefore be affected by numerical resolution. This uncertainty has little direct impact on the final stellar mass budget, since stars around $\sim 10^2$ $M_\odot$ account for only ~ 1 % of the total stellar mass in Figure 12.

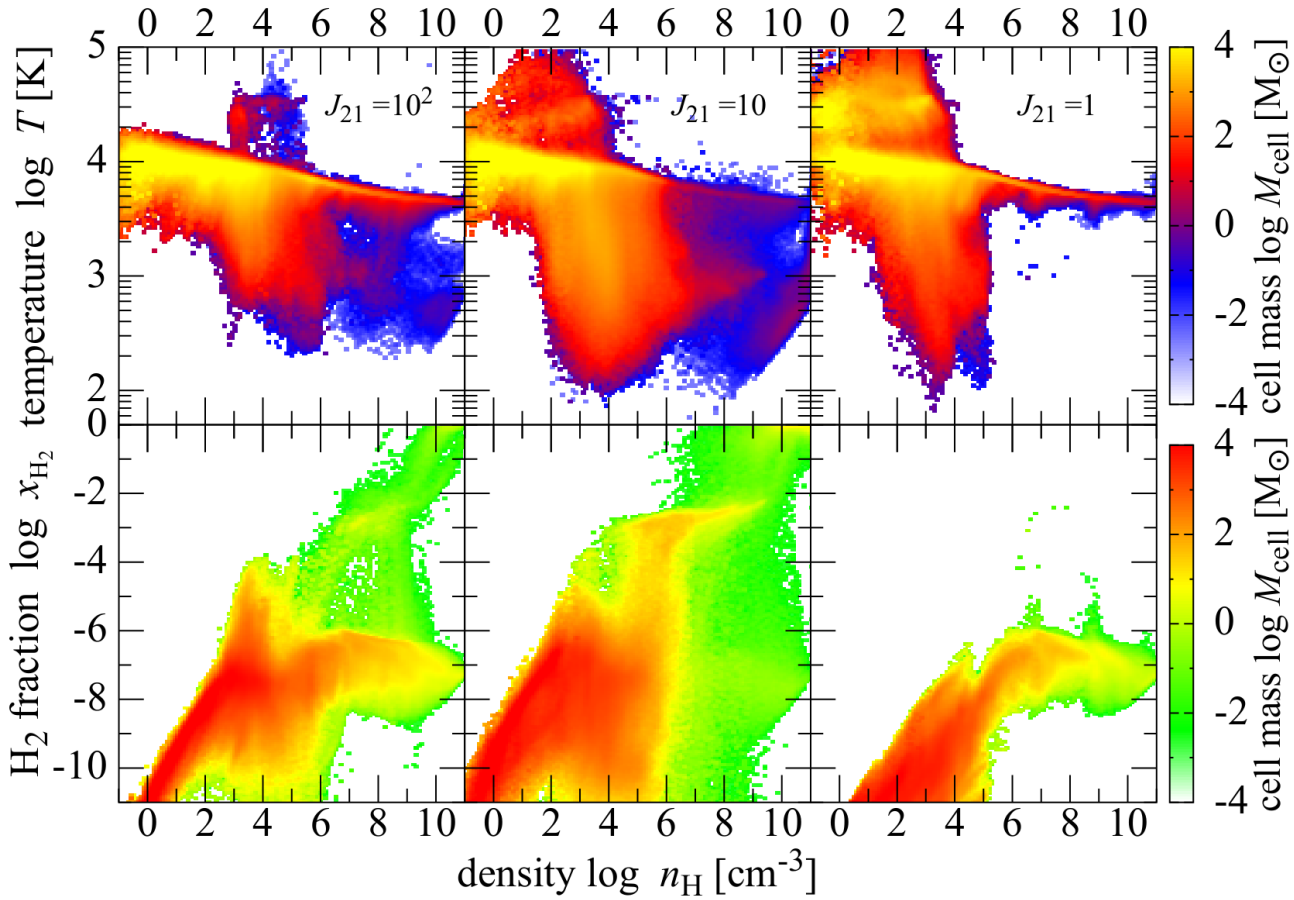


Figure 8. Gas mass distributions on the density–temperature (top) and density–H_2 fraction (bottom) planes at the onset of star formation induced by the global collapse for the different runs. From left to right, the panels correspond to the $J_{21} = 10^2$, 10, and 1 runs at $t = 0.86$, 0.73, and 1.95 Myr, respectively. The horizontal axis shows the gas number density, n_H, while the vertical axis shows the temperature (top) or H_2 fraction (bottom). The colour scale indicates the gas mass contained in each bin.

We also note that unresolved fragmentation during the initial star-formation episode could indirectly affect the subsequent evolution by altering the strength of radiative feedback. More efficient fragmentation into lower-mass stars would reduce the radiative output per unit stellar mass, requiring a larger total stellar mass to build up before radiative feedback becomes strong enough to suppress further fragmentation driven by H_2 cooling. The resulting increase in the total stellar mass may partially compensate for the reduced radiative output per unit stellar mass.

4 DISCUSSION

The results presented above suggest a pathway to SMS formation that does not require the extremely strong external FUV irradiation assumed in the conventional direct-collapse scenario. Once the first Pop III stars form, their internal radiative feedback can suppress H_2 cooling and trigger the global collapse of the surrounding atomic-cooling gas.

In the following, we discuss the subsequent growth and fate of the most massive stars (Section 4.1), their implications for LRDs and SMBHs (Section 4.2), the accompanying compact stellar component (Section 4.3), comparisons with previous studies (Section 4.4), and possible transient signatures (Section 4.5).

4.1 Subsequent growth and fate of the most massive stars

In this subsection, we estimate the possible final masses of the most massive stars and discuss their eventual evolution into massive BHs. The simulations end while these stars are still growing: they have reached $m_\star \sim 10^4$ M$_\odot$ and continue to accrete at high rates (see Section 3.1). Their subsequent growth and final fate therefore remain uncertain.

The high accretion rates found in our simulations suggest that the most massive stars can continue to grow without being strongly limited by their own ionizing feedback. Their typical accretion rates are $\dot{m}_\star \sim 0.1$–1 M$_\odot$ yr^{-1} (Figure 3), well above the critical value $\dot{m}_{\rm crit} \simeq 0.04$ M$_\odot$ yr^{-1} above which rapidly accreting protostars remain inflated and their UV feedback is strongly suppressed. At such high accretion rates, the effective temperature stays as low as $T_{\rm eff} \sim 5000$ K, making ionizing feedback from the star itself weak and allowing rapid accretion to continue (Hosokawa et al. 2012). If maintained for ~ 1 Myr, the accretion rates measured in our simulations would allow the stars to grow to $\gtrsim 10^5$ M$_\odot$.

If rapid accretion continues, the stars remain in the SMS phase until they eventually collapse after exhausting their nuclear fuel or becoming unstable to general-relativistic effects. Their final masses depend on the accretion rate and can be approximated as

$$m_{\star,\rm final} \simeq \left[0.83\left(\frac{\dot{m}_\star}{1\ {\rm M}_\odot\ {\rm yr}^{-1}}\right) + 2.48\right] \times 10^5\ {\rm M}_\odot \quad (12)$$

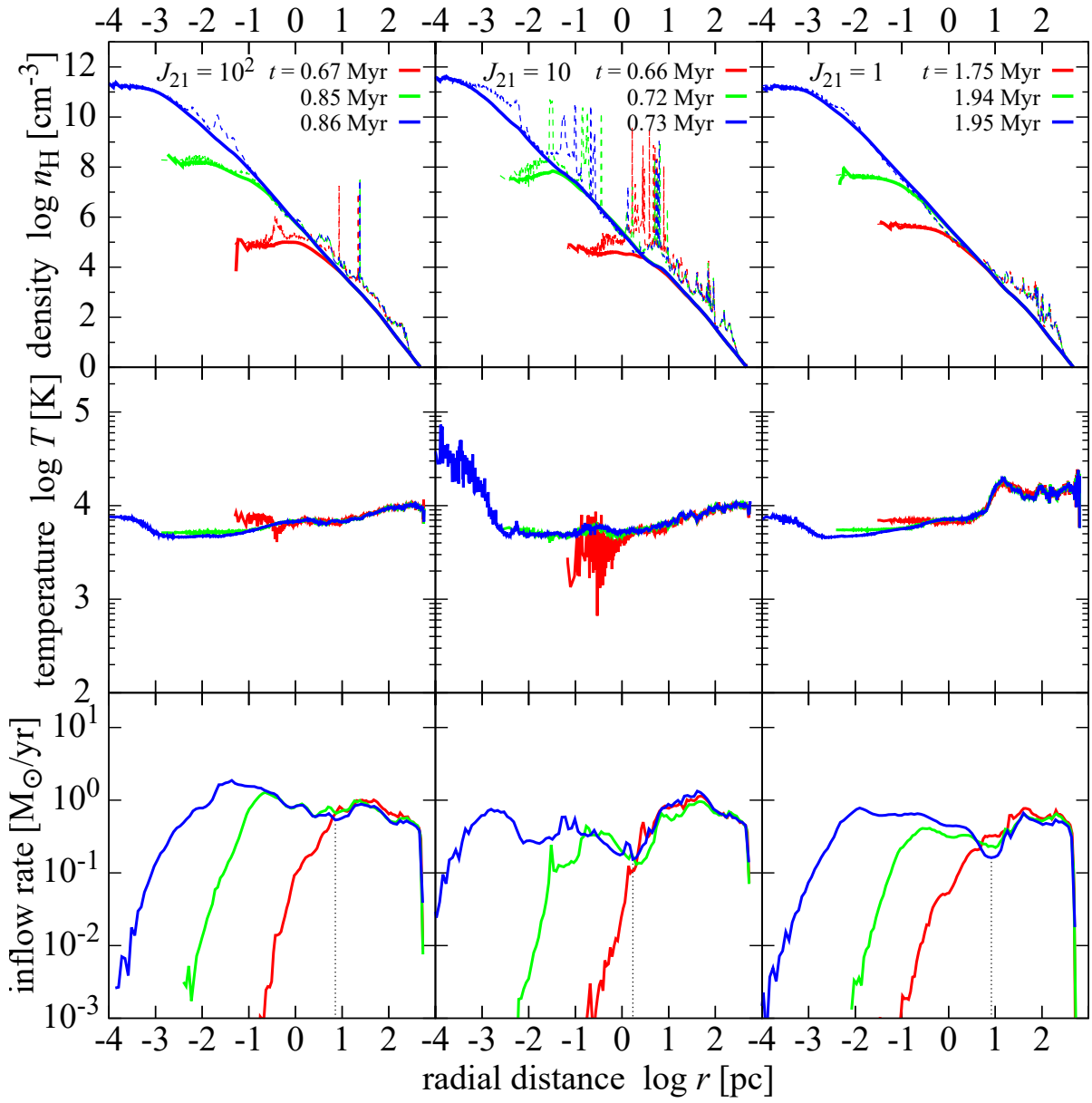


Figure 9. Time evolution of the radial structure of the collapsing gas for the different runs. From left to right, the panels correspond to the $J_{21} = 10^2$, 10, and 1 runs. The horizontal axis shows the radial distance from the density peak. Red, green, and blue curves represent progressively later epochs, with the blue curves corresponding to the epoch immediately before star formation associated with the global collapse. *Top row:* Gas density. Dashed curves show the mass-weighted mean density within each radial bin, while solid curves show the enclosed mean density, $\bar{n}_{\rm H} = 3M_{\rm gas}(< r)/(4\pi r^3 \mu m_{\rm H})$. *Middle row:* Gas temperature, shown as the mass-weighted mean within each radial bin. *Bottom row:* Gas mass inflow rate. Dashed vertical lines mark the radii of the local minima in the inflow-rate profiles at this epoch; the regions inside these radii are defined as the global-collapse regions (see text).

(Woods et al. 2017). Applying this relation to the mean accretion rates found in our simulations gives final stellar masses of $\sim$ few$\times 10^5$ M$_\odot$. These estimates should be regarded as optimistic, as they assume that the gas reservoir remains available and that high accretion rates are sustained throughout the lifetime of the SMSs.

The actual mass growth may terminate before these upper limits are reached because of feedback from the surrounding stellar population. Photoionization feedback is unlikely to significantly impede the large-scale gas supply, whereas supernova feedback may become important on a timescale of $\sim$ 2 Myr.

The global-collapse region contains not only SMSs but also numerous massive stars with $m_\star \sim 10^2$ M$_\odot$. Ionizing radiation from these stars heats the surrounding gas, but the high recombination rate in the dense collapsing envelope confines the ionized regions to scales of order a few pc (see Appendix A).

Supernova feedback is not included in the present simulations. Massive Pop III stars with $m_\star \gtrsim 10^2$ M$_\odot$ have characteristic lifetimes of $\sim$ 2 Myr (e.g. Schaerer 2002), after which supernova explosions may affect the central gas reservoir. Their impact cannot be determined from our simulations. We therefore consider two limiting estimates, referred to below as the conservative and optimistic cases.

In the conservative case, we assume that supernova feedback terminates further stellar growth at $t = 2$ Myr. We extrapolate the stellar growth to this time using the mean accretion rates inferred

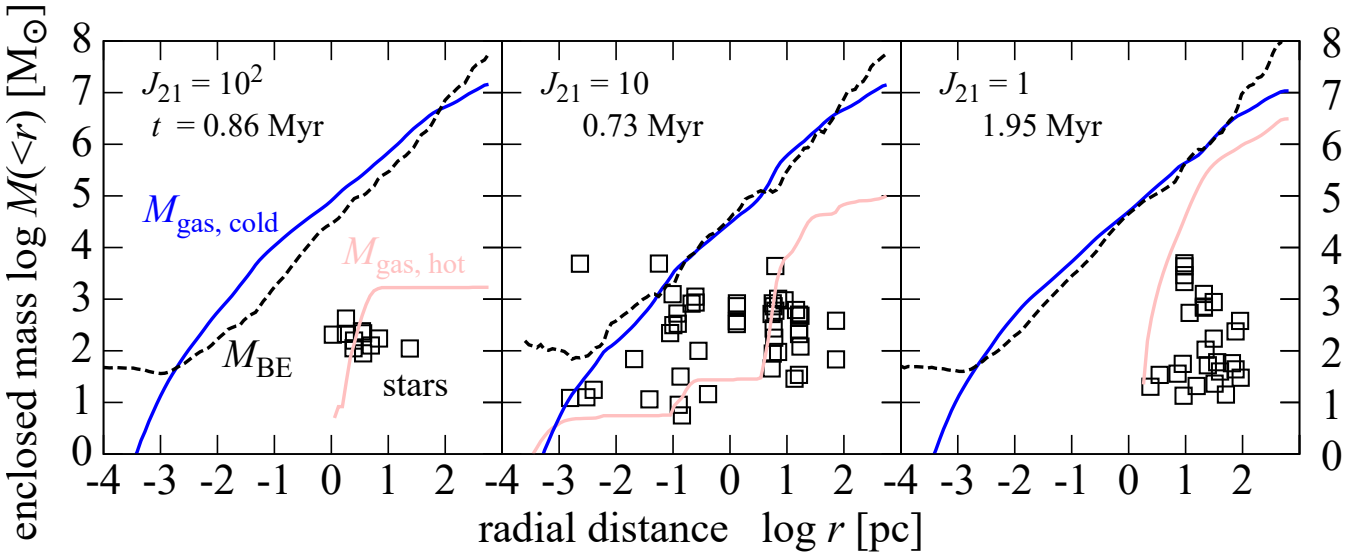


Figure 10. Radial profiles of the enclosed gas mass at the onset of star formation associated with the global collapse for the different runs. From left to right, the panels correspond to the $J_{21} = 10^2$, 10, and 1 runs. The horizontal axis shows the radial distance from the density peak, and the vertical axis shows the enclosed gas mass. The blue and pink lines show the enclosed masses of the cold ($T < 2 \times 10^4$ K) and hot ($T > 2 \times 10^4$ K) gas, respectively. The black dashed lines show the Bonnor–Ebert mass evaluated using the properties of the cold gas. Square symbols indicate the positions and masses of the star particles.

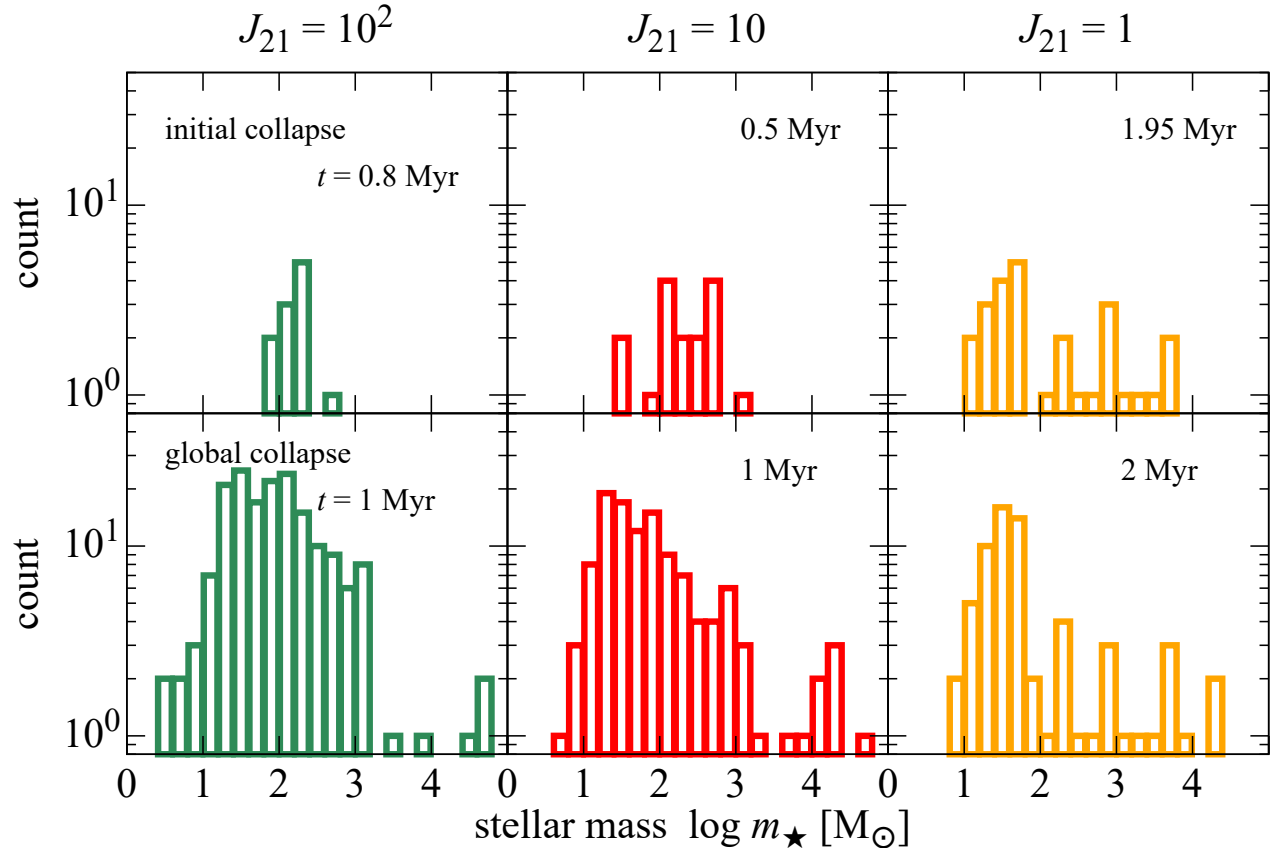


Figure 11. Stellar mass distributions for the different runs. The horizontal axis shows the stellar mass, $m_\star$, and the vertical axis shows the number of stars in each mass bin. From left to right, the panels correspond to the $J_{21} = 10^2$, 10, and 1 runs. *Top row:* Mass distributions resulting from star formation during the initial-collapse phase, shown immediately before star formation associated with the global collapse. *Bottom row:* Mass distributions at the end of each simulation, following the global-collapse phase.

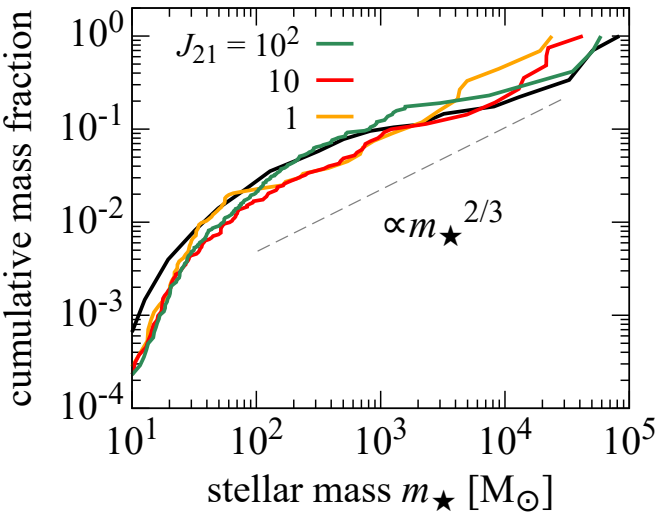


Figure 12. Cumulative stellar mass fraction at the final epoch of each run. The horizontal axis shows the stellar mass, $m_\star$, and the vertical axis shows the cumulative stellar mass fraction, $M_{\rm cum}(< m_\star)/M_{\rm tot}$. The green, red, and orange lines correspond to the $J_{21} = 10^2$, 10, and 1 runs, respectively. The black line shows the corresponding distribution for the $J_{21} = 10^3$ run of Chon & Omukai (2025). The grey dashed line indicates a reference slope proportional to $m_\star^{2/3}$, with arbitrary normalization.

Table 2. Estimated final masses of the most massive stars. In the conservative case, accretion is extrapolated to $t = 2$ Myr, when supernova feedback is assumed to terminate further growth, with the final mass capped at the upper limit given by equation (12). In the optimistic case, accretion is assumed to continue until the upper mass limit given by equation (12) is reached.

Run	$\langle \dot{m}_\star \rangle$ [$M_\odot$ yr^{-1}]	$m_{*,\rm final}$ (conservative) [$M_\odot$]	$m_{*,\rm final}$ (optimistic) [$M_\odot$]
$J_{21} = 10^2$	0.41	2.8×10^5	2.8×10^5
$J_{21} = 10$	8.1×10^{-2}	1.0×10^5	2.5×10^5
$J_{21} = 1$	0.46	2.3×10^4	2.9×10^5

from Figure 3. If the extrapolated mass exceeds the upper limit given by equation (12), we adopt the latter value.

In the optimistic case, we assume that the gas reservoir survives supernova feedback and continues to supply gas to the most massive stars until the upper mass limit given by equation (12) is reached. The resulting final stellar masses are summarized in Table 2.

In the conservative case, whether the most massive stars can reach the $\sim 10^5$ $M_\odot$ scale depends strongly on how early the system enters the SMS formation phase. For the $J_{21} = 10^2$ run, extrapolation to $t = 2$ Myr gives $m_\star \sim 5 \times 10^5$ $M_\odot$. Since this exceeds the upper limit from equation (12), we adopt the value given by that relation. For $J_{21} = 10$, the extrapolated mass reaches $\sim 10^5$ $M_\odot$ by $t = 2$ Myr. In the $J_{21} = 1$ run, the transition to the SMS formation phase occurs much later, at $t = 1.95$ Myr, leaving little time for subsequent growth before the assumed onset of supernova feedback. The extrapolated mass therefore remains close to the value at the end of the simulation, $\sim 2 \times 10^4$ $M_\odot$.

Taken together, these estimates indicate that the most massive stars can reach $m_\star \gtrsim 10^5$ $M_\odot$ if the gas supply persists sufficiently long. Their final masses are determined primarily by whether supernova feedback terminates the gas supply before they reach the stellar-evolution limit given by equation (12).

4.2 Implications for Little Red Dots and the origin of SMBHs

In this subsection, we discuss the implications of our SMS/DCBH formation channel for LRDs and the present-day SMBH population. We first compare the expected BH masses and abundance with those inferred for LRDs, and then compare the estimated DCBH abundance with the number density of present-day SMBHs.

To assess whether the DCBHs formed through our scenario can power LRDs with comparable luminosities, we first estimate their subsequent growth through gas accretion. The SMS collapse is expected to leave a BH containing most of the stellar mass (e.g., Shibata & Shapiro 2002). Figure 10 shows that the self-gravitating gas reservoir surrounding the stellar system extends over $\sim 10^2$ pc and contains $\sim 4 \times 10^6$ $M_\odot$. If this reservoir is not disrupted by radiative or supernova feedback, its ongoing self-gravitating inflow may continue to feed the central BH after SMS collapse (Chon et al. 2026). The fraction of this reservoir ultimately accreted on to the BH is uncertain. For an order-of-magnitude estimate, we adopt an accreted fraction of $\sim 30\%$, motivated by the finding that the most massive star acquires 20–40% of the total stellar mass in our simulations. This gives a BH mass of $\sim 10^6$ $M_\odot$.

This is broadly consistent with the $\sim 10^6$ $M_\odot$ BH mass scale inferred for some LRDs if their emission is powered by accreting BHs (Naidu et al. 2025; Kido et al. 2025; Inayoshi & Maiolino 2025; Begelman & Dexter 2026; de Graaff et al. 2025). However, substantially more massive BHs have also been found in LRDs. In particular, a recent dynamical measurement for A2744-QSO1 indicates $M_{\rm BH} \sim 5 \times 10^7$ $M_\odot$ (Juodžbalis et al. 2026).

We next estimate the cosmological abundance of DCBHs formed through this channel and compare it with the observed abundances of LRDs and present-day SMBHs.

For SMS/DCBH formation through this channel, the gas must remain pristine until the halo reaches the atomic-cooling scale, $M_{\rm halo} \sim 10^8$ $M_\odot$. For this estimate, we classify a halo as non-pristine if star formation occurs in any of its progenitor minihaloes. At external FUV intensities comparable to the cosmological mean background, $J_{21} \sim$ 6–40 (Dijkstra et al. 2008), the merger-tree calculations of Fernandez et al. (2014) give pristine fractions of

$$f_{\rm pristine} \sim 2 \times 10^{-4}, \quad 4 \times 10^{-3}, \tag{13}$$

for $J_{21} = 10$ and 30, respectively.

The abundance of atomic-cooling haloes with $M_{\rm halo} \sim 10^8$ $M_\odot$ at $z \lesssim 10$ is approximately

$$n_{\rm ACH} \sim 10 \ {\rm cMpc}^{-3} \tag{14}$$

(e.g. Barkana & Loeb 2001). Combining this with the pristine fractions estimated above, we obtain

$$n_{\rm DCBH} \sim f_{\rm pristine} n_{\rm ACH} \sim 2 \times 10^{-3}, 4 \times 10^{-2} \ {\rm cMpc}^{-3} \tag{15}$$

for $J_{21} = 10$ and 30, respectively. Thus, even when restricting SMS/DCBH formation to strictly metal-free gas, the expected DCBH number density is $\sim 10^{-3}$–a few $\times 10^{-2}$ cMpc^{-3} under a cosmological-mean FUV background.

We next compare the estimated DCBH abundance with the observed LRD population. LRDs have a number density of $n_{\rm LRD} \sim 10^{-5}$–10^{-4} cMpc^{-3} (Matthee et al. 2024; Pérez-González et al. 2024; Kokorev et al. 2024; Greene et al. 2024), which is well below our estimated DCBH abundance. If only a fraction $f_{\rm duty}$ of DCBHs are observed in an LRD-like active state at any given time, their number densities are related by

$$n_{\rm LRD} \sim f_{\rm duty} n_{\rm DCBH}. \tag{16}$$

Here, $f_{\rm duty}$ denotes the duty cycle of the LRD-like phase. As in

AGN populations more generally, duty cycles are naturally expected to be below unity (Schawinski et al. 2015; Aird et al. 2018). The observed LRD abundance and estimated DCBH abundances then imply a characteristic duty cycle of $f_{\rm duty} \sim 10^{-2}$. If the LRD state corresponds to a single evolutionary phase in the growth of each DCBH, this duty cycle corresponds to a characteristic duration of

$$t_{\rm LRD} \sim f_{\rm duty} t_{\rm H} \sim 10\,{\rm Myr}, \quad (17)$$

where $t_{\rm H} \sim 1$ Gyr is the Hubble time at $z \sim 6$. A duration of ~ 10 Myr is consistent with the picture of LRDs as a transient phase of BH-powered emission during BH growth (Naidu et al. 2025; Kido et al. 2025; Begelman & Dexter 2026).

The inferred duty cycle also has implications for the DCBH occupation fraction of the galaxy population. Comparison between the UV luminosity functions of LRDs and galaxies at $z \sim 5$–6 gives

$$n_{\rm LRD} \sim f_{\rm duty} f_{\rm occ} n_{\rm gal}, \quad (18)$$

with $f_{\rm duty} f_{\rm occ} \sim 10^{-2}$ (Asada et al. 2026), where $f_{\rm occ}$ is the DCBH occupation fraction. If the same duty cycle inferred above applies, $f_{\rm duty} \sim 10^{-2}$ implies an occupation fraction of order unity, $f_{\rm occ} \sim 1$. This would suggest that most galaxies in the luminosity range relevant to LRDs already host heavy seed BHs, while only a small fraction appear as LRDs at any given time.

The inferred DCBH abundance is also comparable to that of SMBHs in the local Universe, $n_{\rm SMBH} \sim 10^{-3}$–$10^{-2}$ cMpc^{-3} (Greene & Ho 2007; Schulze & Wisotzki 2010; Miller et al. 2015; Zou et al. 2025). This suggests that our formation channel can provide a sufficiently abundant progenitor population for present-day SMBHs. Whether individual DCBHs subsequently grow into SMBHs is not addressed here and depends on their gas accretion (Latif et al. 2018; Chon et al. 2021, 2026) and merger histories (Valiante et al. 2016; Trinca et al. 2022; Schneider et al. 2023). Moreover, the pristine fraction depends on the halo mass and redshift, so the DCBH abundance estimated above should be regarded as approximate.

The abundance estimated above may represent a lower limit because DCBH formation is not necessarily restricted to strictly metal-free gas. Under strong FUV irradiation, central objects can grow into SMSs even at metallicities of $Z \lesssim 10^{-3}\,Z_\odot$, despite fragmentation induced by dust cooling (Chon & Omukai 2020, 2025). Cosmological semi-analytic calculations incorporating the super-competitive accretion channel at finite metallicity likewise find an enhanced population of massive BH seeds (Sassano et al. 2021). However, it remains unclear whether the halo-internal irradiation mechanism studied here remains effective under such conditions.

As the metallicity increases, metal cooling causes the gas to depart from the atomic-cooling temperature of several thousand K at progressively lower densities. Fragmentation then occurs at lower densities and on corresondingly larger spatial and mass scales, where the free-fall time is longer. This may delay the reassembly and subsequent global collapse of the gas, allowing stellar feedback to disrupt the cloud before global collapse is completed. Radiation-hydrodynamic simulations including finite metallicity are required to determine whether this formation channel remains viable.

The strong increase in the number of potential formation sites at finite metallicity is also suggested by Chiaki et al. (2023). Combining cosmological N-body simulations with a semi-analytic galaxy model, they estimated the abundance of SMS/DCBH formation sites while following the metallicity and internal and external LW radiation fields of individual haloes. They assumed DCBH formation in atomic-cooling haloes ($T_{\rm vir} > 8000$ K) with $Z < Z_{\rm th}$ and an internal radiation field of $J_{21} > 10^3$. The resulting DCBH number density increases from $n_{\rm DCBH} \simeq 0.03$–0.06 Mpc^{-3} for $Z_{\rm th} \le 10^{-4} Z_\odot$ to $n_{\rm DCBH} \simeq 1$ Mpc^{-3} for $Z_{\rm th} = 10^{-3} Z_\odot$. Although their assumed radiation threshold is much higher than the external FUV intensities considered here, their results illustrate how allowing finite metallicity can substantially increase the abundance of potential SMS/DCBH formation sites.

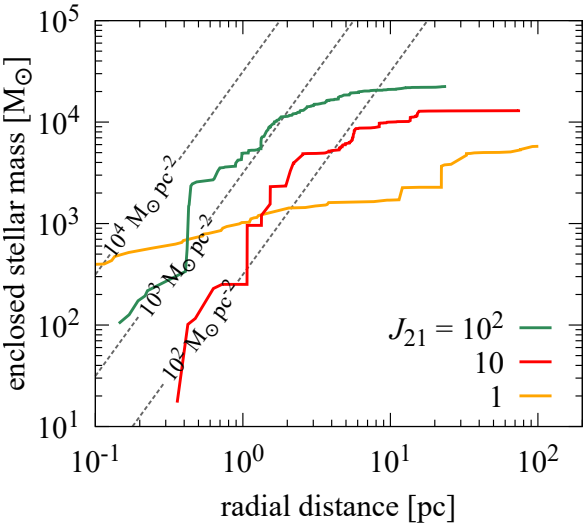


Figure 13. Radial distribution of stars in the final snapshot of each run. The horizontal axis shows the radial distance from the most massive star, and the vertical axis shows the enclosed stellar mass, $M_{\star,\rm enc}$, including only stars with $M_\star < 10^3$ M$_\odot$. The green, red, and orange solid lines correspond to the $J_{21} = 10^2$, 10, and 1 runs, respectively. The grey dashed lines indicate constant stellar surface densities, $\Sigma_\star = M_{\star,\rm enc}/(\pi r^2)$, of 10^2, 10^3, and 10^4 M$_\odot$ pc^{-2}.

4.3 Compact Stellar Systems and Pop III Galaxy Candidates

In this subsection, we compare the compact stellar component formed in our simulations with observed compact stellar systems and candidate Pop III or extremely metal-poor stellar populations at high and intermediate redshifts. We first characterize its spatial extent and stellar surface density directly from the simulations. We then focus on the young massive-star component with $m_\star < 10^3$ M$_\odot$ formed around the SMSs and use simple SED models to estimate the stellar mass required to reproduce the observed UV continuum fluxes and recombination-line luminosities.

To compare the simulated stellar systems with the compact sources observed by JWST, we first determine their characteristic size and the mass of the compact young stellar component that dominates their radiative output. Figure 13 shows the radial distribution of stars with $m_\star < 10^3$ M$_\odot$ in the final snapshot of each run, centred on the most massive star. We define the mass of this component as

$$M_{\star,\rm comp} \equiv M_{\star,\rm tot}(m_\star < 10^3\,{\rm M}_\odot). \quad (19)$$

At the end of the simulations, $M_{\star,\rm comp} \sim 10^4$ M$_\odot$.

This mass may increase if star formation continues beyond the simulated period. The total stellar mass growth rate after the global collapse is ~ 0.1–1 M$_\odot$ yr^{-1}, so sustained star formation for a few Myr could increase the total stellar mass to $\sim 10^6$ M$_\odot$. Assuming that $\sim 10\%$ of this mass remains in stars with $m_\star < 10^3$ M$_\odot$ then gives $M_{\star,\rm comp} \sim 10^5$ M$_\odot$.

Figure 13 shows that the stellar component is compact, extending over $\sim$ 1–10 pc, with most stars concentrated within the central $\lesssim 10$ pc. In the $J_{21} = 10^2$ run, the stellar surface density reaches $\Sigma_\star \gtrsim 10^3$ M$_\odot$ pc^{-2} within $\lesssim 1$ pc. In the $J_{21} = 10$ run, $\Sigma_\star \sim$

10^2 $M_\odot\,pc^{-2}$ within $\lesssim 3$ pc. In the $J_{21} = 1$ run, the simulation is terminated shortly after the onset of star formation induced by the global collapse. Stars with a total mass of ~ 400 $M_\odot$ are already concentrated near the collapse centre, reaching a local stellar surface density of $\sim 10^4$ $M_\odot\,pc^{-2}$. Thus, although the stellar components remain modest in total mass at the end of the simulations, they already form compact stellar systems on pc scales.

We compare the UV continuum and recombination-line luminosities, which are more directly observable than the total stellar mass and less sensitive to the assumed IMF.

We first consider the UV continuum from the compact young stellar component. Based on the metal-free ZAMS models of Schaerer (2002), we approximate the stars in this component as blackbody emitters with $T_{\rm eff} = 10^5$ K and $L_\star = 0.7 L_{\rm Edd}$. These values are representative of $m_\star \sim 500$–1000 $M_\odot$ stars, which dominate the mass and radiative output of this component in our simulations. The total bolometric luminosity is therefore

$$L_{\rm bol} = 0.7 L_{\rm Edd}(M_{\star,\rm comp}) \simeq 1.1\times10^{42}\left(\frac{M_{\star,\rm comp}}{10^4\ M_\odot}\right)\ {\rm erg\ s^{-1}}. \quad (20)$$

Table 3 summarizes the comparison between the characteristic size and $M_{\star,\rm comp}$ of the compact stellar systems in our simulations and those inferred for the observed systems. For each observed object, we list its size and the stellar mass required to reproduce either the UV continuum or recombination-line luminosity.

Overall, the compact stellar systems formed in our simulations have sizes comparable to the pc-scale structures inferred for several JWST sources. The simulated masses, $M_{\star,\rm comp} \sim 10^4$ $M_\odot$, are somewhat smaller than those inferred for several of the observed systems, but continued growth to $\sim$ few $\times\, 10^4$–10^5 $M_\odot$ could reproduce the UV or He II luminosities of sources such as AMORE6 and *Hebe* . The stacked He II luminosity of the HETDEX candidates discussed below requires a substantially larger mass, $M_{\star,\rm comp} \sim 2\times10^6$ $M_\odot$, in our simple model.

4.3.1 *UV continuum*

For the UV continuum comparison, the adopted stellar SED gives

$$M_{\rm UV} \simeq -12.4 - 2.5\log_{10}\left(\frac{M_{\star,\rm comp}}{10^4\ M_\odot}\right). \quad (21)$$

AMORE6 is a strongly lensed, extremely metal-poor galaxy at $z = 5.7253$ (Morishita et al. 2025). It has an intrinsic effective radius of $R_e \simeq 36$ pc and a UV magnitude of $M_{\rm UV} \simeq -14.5$. Its size is somewhat larger than the $\sim$ 1–10 pc extent of the compact stellar systems in our simulations. Reproducing its UV luminosity with our toy SED model requires $M_{\star,\rm comp} \sim 7\times10^4$ $M_\odot$, which could be reached with continued star formation beyond the simulated period.

The Firefly Sparkle is a strongly lensed galaxy at $z_{\rm spec} = 8.296$ containing multiple compact stellar clumps (Mowla et al. 2024). Most individual clumps are unresolved, with lensing-corrected half-light radii of $R_{\rm eff} < 4$–7 pc, comparable to the $\sim$ 1–10 pc extent of the compact stellar systems in our simulations.

For the brightest component, FF-6, reproducing the intrinsic F150W luminosity with our toy SED model requires $M_{\star,\rm comp} \simeq 6\times10^5$ $M_\odot$. This is substantially larger than the current simulation value, $M_{\star,\rm comp} \sim 10^4$ $M_\odot$, and the $\sim 10^5$ $M_\odot$ expected from our extrapolation of continued star formation.

At $z \simeq 10.2$, Adamo et al. (2024) report the discovery of five compact star-cluster candidates, the so-called Cosmic Gems. Their lensing-corrected half-light radii are typically $R_{\rm eff} \sim 1$ pc, comparable to the compact stellar systems formed in our simulations. Their inferred ages of $\sim$ 9–36 Myr are substantially longer than the lifetime of the massive stars considered in our SED model. We therefore use the Cosmic Gems only as a comparison for pc-scale compactness, rather than for their stellar SEDs.

4.3.2 *Recombination-line emission*

We next estimate the He II recombination-line luminosity from the compact stellar component. The metal-free ZAMS models of Schaerer (2002) give an He^+-ionizing photon production rate of $Q(He^+)/m_\star \simeq 2.7\times10^{47}$ s^{-1} $M_\odot^{-1}$ for stars with $m_\star = 500$–1000 $M_\odot$. Adopting this as a representative value for the compact stellar component, we obtain

$$Q(He^+) \simeq 2.7\times10^{51}\left(\frac{M_{\star,\rm comp}}{10^4\ M_\odot}\right) s^{-1}. \quad (22)$$

Using the case-B conversion factor of Schaerer (2002), the He II λ1640 luminosity is

$$L_{\rm HeII} = 5.67\times10^{-12}\left(1-f_{\rm esc,He^+}\right)Q(He^+) \simeq 1.5\times10^{40}\left(1-f_{\rm esc,He^+}\right)\left(\frac{M_{\star,\rm comp}}{10^4\ M_\odot}\right){\rm erg\ s^{-1}}, \quad (23)$$

where, $f_{\rm esc,He^+}$ is the fraction of He^+-ionizing photons. We adopt $f_{\rm esc,He^+} = 0$ as our fiducial value, since these photons are expected to be efficiently absorbed within the compact stellar system. For a non-zero escape fraction, the stellar mass required to reproduce a given He II luminosity increases as $(1-f_{\rm esc,He^+})^{-1}$.

Hebe is an unresolved He II λ1640 emitter at $z \simeq 10.6$ near GN-z11 and has been discussed as a Pop III stellar-cluster candidate because of the absence of detected metal lines (Rusta et al. 2026; Maiolino et al. 2026). Its observed He II λ1640 luminosity is $L_{\rm HeII} \simeq 8.5\times10^{40}$ erg s^{-1}. In our model, reproducing this luminosity requires $M_{\star,\rm comp} \simeq 6\times10^4\left(1-f_{\rm esc,He^+}\right)^{-1}$ $M_\odot$.

Rusta et al. (2026) further decompose the He II emission into two velocity components and identify the C1 as the more pristine Pop III component. Its He II luminosity, $L_{\rm HeII,C1} \simeq 5.1\times10^{40}$ erg s^{-1}, corresponds to $M_{\star,\rm comp} \simeq 3\times10^4\left(1-f_{\rm esc,He^+}\right)^{-1}$ $M_\odot$ in our model. For our fiducial $f_{\rm esc,He^+} = 0$, this estimate is consistent with the Pop III stellar mass inferred from the more detailed spectral modelling of Rusta et al. (2026).

These masses are only a factor of $\sim$ 3–6 larger than the current simulation value of $M_{\star,\rm comp} \sim 10^4$ $M_\odot$. Continued star formation after the global collapse could therefore produce He II luminosities comparable to those of C1 and *Hebe* as a whole.

Mirza Khanlari et al. (2026) recently identified eight candidate very metal-poor or Pop III-like systems at $z \simeq 2$ from the HETDEX Lyα emitter sample. Their stacked spectrum shows strong He II λ1640 emission, $L_{\rm HeII} \simeq 3.0\times10^{42}$ erg s^{-1}, with no significant N V, C IV, or O III] emission. Applying equation (23) to the stacked He II luminosity gives $M_{\star,\rm comp} \simeq 2\times10^6\left(1-f_{\rm esc,He^+}\right)^{-1}$ $M_\odot$. This mass is substantially larger than both the current stellar mass in our simulations and our optimistic extrapolation assuming continued star formation. The spatial extent of the He II-emitting component is not constrained by the HETDEX data.

LAP1-B is an extremely metal-poor subcomponent of the LAP1 system at $z \simeq 6.64$ (Vanzella et al. 2023). Its Hα-emitting region has a characteristic size of only a few pc, comparable to the compact stellar systems in our simulations. The observed Hα luminosity corresponds to $M_{\star,\rm comp} \sim 10^3$ $M_\odot$ in our model, smaller than the current

simulation value of $\sim 10^4$ $M_\odot$. No secure He II detection is available, preventing a similar comparison of the He^+-ionizing output.

4.4 Comparison with Previous Studies

Our main result is that SMS formation can occur under moderate external FUV irradiation even after H_2 cooling has already triggered fragmentation and Pop III star formation. Radiative feedback from these stars subsequently suppress H_2 cooling in the surrounding atomic-cooling gas, leading to its global collapse on a timescale of $\sim$ 1–2 Myr. Previous studies provide useful comparisons for different stages and aspects of this evolution.

Regan et al. (2020) followed a primordial atomic-cooling halo exposed to a moderate FUV field for $\sim$ 2 Myr. They also find the formation of very massive stars, including one reaching $\sim$ 6000 $M_\odot$, but their accretion rates decline as the local gas reservoirs are depleted. Unlike in our simulations, the fragmented gas does not subsequently reassemble into a coherent $\sim$ 10 pc reservoir and undergo global collapse. The origin of this difference remains unclear, although one potentially important distinction is that ionizing feedback was not dynamically coupled to the gas in their simulations.

Latif et al. (2021) likewise found H_2 cooling leads to the formation of dense clumps and massive stars with $m_\star \sim 10^3$–10^4 $M_\odot$ in atomic-cooling haloes exposed to $J_{21} < J_{\rm crit}$. Several of their simulations were terminated after the accretion rates onto the initially formed stars declined, before the subsequent evolution of the surrounding gas reservoir could be followed. Our results show that the residual reservoir can continue to contract and eventually undergo global collapse.

Kiyuna et al. (2024) found a closely related pathway in which SMS formation occurs under a moderate external FUV field through halo-internal radiative feedback. The main difference is the trigger and timescale of the SMS-forming collapse. In their simulation, SMS formation occurs after a $\sim$ 10–30 Myr quiescent phase and is triggered by a later cosmological cold-accretion flow. In our simulations, the residual atomic-cooling reservoir instead undergoes global collapse within $\sim$ 1–2 Myr, without requiring a later cold-accretion event to trigger the collapse.

Sullivan et al. (2025) found that halo-internal FUV radiation suppresses H_2 cooling in a neighbouring $\sim 10^3$ $M_\odot$ clump, reducing its accretion rate and limiting the stellar mass to $\sim 10^2$–10^3 $M_\odot$. Similar suppression of H_2 cooling occurs in the initially fragmented clumps in our simulations. The SMSs in our simulations, however, form later through the global collapse of the much larger $\sim$ 10 pc, $\sim 10^5$–10^6 $M_\odot$ atomic-cooling reservoir. Thus, while internal radiative feedback suppresses stellar growth on clump scales, it can subsequently promote SMS formation through the global collapse of the surrounding reservoir.

4.5 Possible Transient Signatures

The stellar systems formed in our simulations contain SMS progenitors together with numerous surrounding stars. After the SMSs collapse into massive BHs, these systems may produce electromagnetic and gravitational-wave transients through tidal disruption events (TDEs) and mergers of massive BH binaries (Fialkov & Loeb 2017; Kar Chowdhury et al. 2024).

The lower-mass stars formed around the SMSs, whose lifetimes exceed that of the SMS progenitor, provide potential sources of TDEs after the SMS collapses into a DCBH. In the compact stellar systems expected around newly formed DCBHs, dynamical relaxation can scatter such stars onto loss-cone orbits on a timescale shorter than their lifetimes. Few-body interactions may provide an additional channel for bringing stars close to the DCBH. Such tidal disruptions can produce luminous transients, including long-duration soft X-ray emission accompanied by relativistic jets and radio afterglows (Kashiyama & Inayoshi 2016).

The potential TDE sources in our simulations span a range of stellar masses, although the most massive stars are unlikely to survive until after DCBH formation. The peak fallback rate and jet luminosity scale approximately as

$$\dot{M}_{\rm fb,peak},\ L_j \quad \propto \quad m_\star^2 R_\star^{-3/2} \tag{24}$$

(Stone et al. 2013). Surviving stars at the higher-mass end could therefore produce higher peak fallback rates and more luminous X-ray and radio transients, provided that they remain compact. For bloated protostars, however, their larger radii would increase the fallback timescale and reduce the peak fallback rate and luminosity.

Our simulations also form multiple SMSs rather than a single SMS, so several massive BHs may remain within the same halo after stellar collapse. Recent JWST observations have identified candidate systems containing multiple accreting BHs or closely separated LRDs within individual high-redshift galaxies (Übler et al. 2026; Yanagisawa et al. 2026), suggesting that such multiple-BH configurations may occur at early cosmic times. If the BHs formed in our scenario subsequently form binaries and merge, they would constitute a potential source of gravitational waves. For example, in the $J_{21} = 10^2$ run, the two most massive stars at the end of the simulation form a gravitationally bound pair with masses of 6×10^4 $M_\odot$ and 5×10^4 $M_\odot$, separated by $\sim$ 0.04 pc. Both stars are still growing, so the resulting BH masses may reach $\sim 5 \times 10^4$–10^5 $M_\odot$. This separation is much larger than the ~ 3–5×10^{-4} pc required for a circular binary to merge through gravitational-wave emission within a Hubble time. Additional hardening through gas drag, dynamical friction, stellar scattering, or few-body interactions is therefore required before merger. Nevertheless, the formation of a bound pair of massive BH progenitors demonstrates that the DCBH formation channel considered here can naturally provide initial conditions for high-redshift massive-BH mergers.

The SMSs formed in our simulations are expected to leave BHs with masses of $\sim 10^4$–10^5 $M_\odot$. Mergers of heavy-seed BHs in this mass range may be detectable with future space-based gravitational-wave observatories such as the Laser Interferometer Space Antenna (LISA) and TianQin (Sesana et al. 2007; Klein et al. 2016; Wang et al. 2019). Their mass and mass-ratio distributions may also help distinguish among different BH-seed formation scenarios (Sesana et al. 2007; Klein et al. 2016).

High-redshift TDEs and gravitational-wave mergers may therefore provide complementary observational probes of the DCBH formation channel considered here.

5 CONCLUSION

In this study, we used cosmological radiation-hydrodynamic simulations to follow the evolution of an atomic-cooling halo for $\sim$ 1–2 Myr after the onset of star formation. We focused on how internal radiative feedback from stars formed during the initial star-formation phase affects the subsequent gas dynamics, clustered star formation, and supermassive star (SMS) formation under subcritical external FUV backgrounds of $J_{21} = 1$–10^2.

Our main results are summarized as follows.

Table 3. Summary of the comparison between the compact stellar components in our simulations and observed compact metal-poor systems. For our simulations, the first row shows the current snapshots, while the second gives an optimistic extrapolation assuming continued star formation for a few Myr. For the observed systems, $M_{\star,\mathrm{comp}}$ is the stellar mass required to reproduce the indicated observable using the simple models adopted in this work, rather than the stellar mass inferred in the original observational studies.

Object	Radius [pc]	Observable	$M_{\star,\mathrm{comp}}$ [$\mathrm{M}_\odot$]
This work	$\sim$ 1–10	simulation snapshot	$\sim 10^4$
This work (continued star formation)	—	optimistic extrapolation	$\sim 10^5$
AMORE6 (Morishita et al. 2025)	$\sim$ 36	UV continuum	$\sim 7 \times 10^4$
The Firefly Sparkle FF-6 (Mowla et al. 2024)	$<$ 4–7	F150W continuum	$\sim 6 \times 10^5$
Cosmic Gems (Adamo et al. 2024)	$\sim$ 1	—	—
Hebe (total) (Rusta et al. 2026; Maiolino et al. 2026)	$<$ 400	He II λ1640	$\sim 6 \times 10^4$
Hebe C1 (Rusta et al. 2026)	$<$ 400	He II λ1640	$\sim 3 \times 10^4$
HETDEX He II stack (Mirza Khanlari et al. 2026)	—	He II λ1640	$\sim 2 \times 10^6$
LAP1-B (Vanzella et al. 2023)	$<$ 5	Hα	$\sim 10^3$

- In all runs, star formation in the atomic-cooling halo proceeds through a characteristic two-stage evolution. The gas first undergoes an initial collapse driven by H_2 cooling, similar to ordinary Pop III star formation. Internal radiative feedback from the stars formed during this phase then suppresses H_2 cooling and small-scale fragmentation, while the surrounding atomic-cooling gas reservoir contracts under self-gravity and undergoes global collapse.
- The global collapse involves a gravitationally bound gas reservoir extending over $\sim$ 10–100 pc. It leads to the formation of protostars with high accretion rates of $\sim$ 0.1–1 $\mathrm{M}_\odot\,\mathrm{yr}^{-1}$, with the most massive objects reaching $\sim 10^4$ $\mathrm{M}_\odot$ by the end of the simulations. Their accretion rates remain well above the critical value $\simeq 0.04\,\mathrm{M}_\odot\,\mathrm{yr}^{-1}$ required to maintain the inflated supergiant-protostar state. Since accretion is still ongoing, these objects are expected to grow further toward $\sim 10^5$ $\mathrm{M}_\odot$ and become SMSs.
- The global collapse is not monolithic but is accompanied by clustered star formation. Numerous stars with $m_\star \lesssim 10^3$ $\mathrm{M}_\odot$ form, but $\sim$ 90% of the stellar mass accreted during this phase is concentrated in a small number of rapidly accreting protostars with $m_\star \gtrsim 10^4$ $\mathrm{M}_\odot$. The resulting stellar system can therefore be characterized as a strongly top-heavy system containing a few central SMSs surrounded by a compact young stellar component.
- The SMSs formed through this pathway are expected to leave DCBHs with masses of $\sim 10^5$ $\mathrm{M}_\odot$, which could grow further through accretion from the surrounding gas reservoir. The estimated abundance of these DCBHs, $n_{\mathrm{DCBH}} \sim 10^{-3}$–$10^{-2}$ cMpc^{-3}, is sufficiently high to provide a plausible progenitor population for BH-powered LRDs and present-day SMBHs.
- The global collapse forms not only SMSs but also a compact young stellar component concentrated within $\sim$ 1–10 pc. Its stellar mass reaches $\sim 10^4$ $\mathrm{M}_\odot$ by the end of the simulations and could grow further with continued star formation. Its compactness, together with the expected UV and recombination-line emission, suggests a possible connection to compact metal-poor and Pop III candidates observed with JWST. The global-collapse scenario may therefore be relevant not only to heavy-seed BH formation but also to the formation of compact stellar systems in the early Universe.

These results show that, even under subcritical external FUV backgrounds, radiative feedback from stars formed earlier within an atomic-cooling halo can induce large-scale gas collapse and SMS formation. The process simultaneously produces a small number of SMSs that dominate the stellar mass budget and a compact young stellar component capable of producing observable UV continuum and recombination-line emission. The global-collapse scenario proposed here may therefore provide a common framework linking SMS formation, DCBH formation, high-redshift compact Pop III systems, and the LRD population discovered with JWST.

Future simulations including supernova feedback, BH accretion feedback, metal enrichment, and longer-term evolution will be required to determine the final masses of the SMS progenitors, the subsequent evolution of the stellar population after the global collapse, the mass supply onto the DCBHs, and their observational signatures.

ACKNOWLEDGEMENTS

We would like to thank Kazumi Kashiyama, Takashi Hosokawa, Kazuyuki Sugimura, Daisuke Toyouchi, Kazutaka Kimura, Ryunosuke Maeda, and Tomoya Suzuguchi for fruitful discussions and helpful comments. Numerical computations were carried out on the Cray XD2000 system Aterui II at the Center for Computational Astrophysics, National Astronomical Observatory of Japan. This work was supported by Grants-in-Aid for Scientific Research from the Ministry of Education, Culture, Sports, Science and Technology (MEXT) of Japan under Grant Nos. 22H00149 and 26H02060 (KO). This work was supported by the Tohoku University NEXUS Research Fellow Program. RS acknowledges support from the MUR projects FIS-2024-01621 DAWN and PRIN 2022CB3PJ3-FLAGS, the EU Recovery Fund PNRR, and the INFN TEONGRAV initiative.

DATA AVAILABILITY

The data underlying this article will be shared on a reasonable request of the corresponding author.

REFERENCES

Adamo A., et al., 2024, Nature, 632, 513
Aird J., Coil A. L., Georgakakis A., 2018, MNRAS, 474, 1225
Akins H. B., et al., 2025, ApJ, 991, 37
Asada Y., Inayoshi K., Fei Q., Fujimoto S., Willott C. J., 2026, ApJ, 1005, L22
Barkana R., Loeb A., 2001, PhysRep, 349, 125
Bate M. R., Burkert A., 1997, MNRAS, 288, 1060
Begelman M. C., Dexter J., 2026, ApJ, 996, 48

Bromm V., Loeb A., 2003, ApJ, 596, 34
Bromm V., Yoshida N., 2011, ARAA, 49, 373
Bullock J. S., Dekel A., Kolatt T. S., Kravtsov A. V., Klypin A. A., Porciani C., Primack J. R., 2001, ApJ, 555, 240
Chiaki G., Chon S., Omukai K., Trinca A., Schneider R., Valiante R., 2023, MNRAS, 521, 2845
Chon S., Latif M. A., 2017, MNRAS, 467, 4293
Chon S., Omukai K., 2020, MNRAS, 494, 2851
Chon S., Omukai K., 2025, MNRAS, 539, 2561
Chon S., Hirano S., Hosokawa T., Yoshida N., 2016, ApJ, 832, 134
Chon S., Hosokawa T., Yoshida N., 2018, MNRAS, 475, 4104
Chon S., Hosokawa T., Omukai K., 2021, MNRAS, 502, 700
Chon S., Hirano S., Ishiyama T., Chang S.-J., Springel V., 2026, arXiv e-prints, p. arXiv:2601.04955
Dijkstra M., Haiman Z., Mesinger A., Wyithe J. S. B., 2008, MNRAS, 391, 1961
Dunn G., Bellovary J., Holley-Bockelmann K., Christensen C., Quinn T., 2018, ApJ, 861, 39
Fan X., Bañados E., Simcoe R. A., 2023, ARA&A, 61, 373
Fernandez R., Bryan G. L., Haiman Z., Li M., 2014, MNRAS, 439, 3798
Fialkov A., Loeb A., 2017, MNRAS, 471, 4286
Foster P. N., Chevalier R. A., 1993, ApJ, 416, 303
Greene J. E., Ho L. C., 2007, ApJ, 667, 131
Greene J. E., et al., 2024, ApJ, 964, 39
Greif T. H., Johnson J. L., Klessen R. S., Bromm V., 2008, MNRAS, 387, 1021
Habouzit M., Volonteri M., Latif M., Dubois Y., Peirani S., 2016, MNRAS, 463, 529
Hirano S., Bromm V., 2017, MNRAS, 470, 898
Hosokawa T., Omukai K., 2009, ApJ, 691, 823
Hosokawa T., Omukai K., Yorke H. W., 2012, ApJ, 756, 93
Inayoshi K., Maiolino R., 2025, ApJ, 980, L27
Inayoshi K., Visbal E., Haiman Z., 2020, ARAA, 58, 27
Johnson J. L., Greif T. H., Bromm V., 2008, MNRAS, 388, 26
Juodžbalis I., et al., 2026, Nature, 653, 1017
Kar Chowdhury R., Chang J. N. Y., Dai L., Natarajan P., 2024, ApJ, 966, L33
Kashiyama K., Inayoshi K., 2016, ApJ, 826, 80
Kido D., Ioka K., Hotokezaka K., Inayoshi K., Irwin C. M., 2025, arXiv e-prints, p. arXiv:2505.06965
Kitsionas S., Whitworth A. P., 2002, MNRAS, 330, 129
Kiyuna M., Hosokawa T., Chon S., 2024, MNRAS, 534, 3916
Klein A., et al., 2016, Phys. Rev. D, 93, 024003
Klessen R. S., Glover S. C. O., 2023, ARA&A, 61, 65
Kokorev V., et al., 2024, ApJ, 968, 38
Larson R. B., 1969, MNRAS, 145, 271
Latif M. A., Volonteri M., Wise J. H., 2018, MNRAS, 476, 5016
Latif M. A., Khochfar S., Schleicher D., Whalen D. J., 2021, MNRAS, 508, 1756
Maiolino R., et al., 2024a, Nature, 627, 59
Maiolino R., et al., 2024b, A&A, 687, A67
Maiolino R., et al., 2024c, A&A, 691, A145
Maiolino R., et al., 2026, MNRAS, 548, staf2109
Matthee J., et al., 2024, ApJ, 963, 129
Miller B. P., Gallo E., Greene J. E., Kelly B. C., Treu T., Woo J.-H., Baldassare V., 2015, ApJ, 799, 98
Mirza Khanlari M., et al., 2026, arXiv e-prints, p. arXiv:2609.16134
Morishita T., Liu Z., Stiavelli M., Treu T., Bergamini P., Zhang Y., 2025, arXiv e-prints, p. arXiv:2507.10521
Mowla L., et al., 2024, Nature, 636, 332
Naidu R. P., et al., 2025, arXiv e-prints, p. arXiv:2503.16596
Nakajima K., et al., 2026, Nature, 653, 363
Oh S. P., Haiman Z., 2002, ApJ, 569, 558
Omukai K., 2000, ApJ, 534, 809
Omukai K., 2001, ApJ, 546, 635
Omukai K., Schneider R., Haiman Z., 2008, ApJ, 686, 801
Onoue M., et al., 2023, ApJ, 942, L17
Pawlik A. H., Milosavljević M., Bromm V., 2011, ApJ, 731, 54
Pawlik A. H., Schaye J., Dalla Vecchia C., 2015, MNRAS, 451, 1586
Penston M. V., 1969, MNRAS, 144, 425
Pérez-González P. G., et al., 2024, ApJ, 968, 4
Planck Collaboration et al., 2014, A&A, 571, A16
Regan J., Volonteri M., 2024, arXiv e-prints, p. arXiv:2405.17975
Regan J. A., Visbal E., Wise J. H., Haiman Z., Johansson P. H., Bryan G. L., 2017, Nature Astronomy, 1, 0075
Regan J. A., Wise J. H., Woods T. E., Downes T. P., O'Shea B. W., Norman M. L., 2020, The Open Journal of Astrophysics, 3, 15
Rusta E., et al., 2026, ApJ, 1003, L14
Sassano F., Schneider R., Valiante R., Inayoshi K., Chon S., Omukai K., Mayer L., Capelo P. R., 2021, MNRAS, 506, 613
Schaerer D., 2002, A&A, 382, 28
Schawinski K., Koss M., Berney S., Sartori L. F., 2015, MNRAS, 451, 2517
Schneider R., Valiante R., Trinca A., Graziani L., Volonteri M., Maiolino R., 2023, MNRAS, 526, 3250
Schulze A., Wisotzki L., 2010, A&A, 516, A87
Sesana A., Volonteri M., Haardt F., 2007, MNRAS, 377, 1711
Shang C., Bryan G. L., Haiman Z., 2010, MNRAS, 402, 1249
Shibata M., Shapiro S. L., 2002, ApJ, 572, L39
Stone N., Sari R., Loeb A., 2013, MNRAS, 435, 1809
Sugimura K., Omukai K., Inoue A. K., 2014, MNRAS, 445, 544
Sugimura K., Ricotti M., Park J., Garcia F. A. B., Yajima H., 2024, ApJ, 970, 14
Sullivan J., Haiman Z., Kulkarni M., Visbal E., 2025, MNRAS, 542, 822
Trinca A., Schneider R., Valiante R., Graziani L., Zappacosta L., Shankar F., 2022, MNRAS, 511, 616
Übler H., et al., 2026, A&A, 712, A80
Valiante R., Schneider R., Volonteri M., Omukai K., 2016, MNRAS, 457, 3356
Valiante R., Schneider R., Graziani L., Zappacosta L., 2018, MNRAS, 474, 3825
Vanzella E., et al., 2023, ApJ, 945, 53
Visbal E., Haiman Z., Bryan G. L., 2014, MNRAS, 445, 1056
Wang H.-T., et al., 2019, Phys. Rev. D, 100, 043003
Wise J. H., Abel T., 2007, ApJ, 665, 899
Wise J. H., Regan J. A., O'Shea B. W., Norman M. L., Downes T. P., Xu H., 2019, Nat, 566, 85
Wolcott-Green J., Haiman Z., Bryan G. L., 2011, MNRAS, 418, 838
Woods T. E., Heger A., Whalen D. J., Haemmerlé L., Klessen R. S., 2017, ApJ, 842, L6
Yanagisawa H., et al., 2026, arXiv e-prints, p. arXiv:2601.06015
Yoshida N., Abel T., Hernquist L., Sugiyama N., 2003, ApJ, 592, 645
Zou F., et al., 2025, ApJ, 992, 176
de Graaff A., et al., 2025, arXiv e-prints, p. arXiv:2511.21820

APPENDIX A: PHOTOIONIZATION FEEDBACK ON THE GLOBAL-COLLAPSE GAS RESERVOIR

In Section 4.1, we discussed whether accretion onto the most massive stars can continue beyond the end of the simulations. One potential limitation is photoionization feedback from the surrounding massive stars formed during the global collapse. Their ionizing radiation could photoevaporate the dense gas reservoir and reduce the mass supply from larger scales. Here, we estimate whether their ionizing photon emissivity is sufficient to ionize the surrounding dense envelope out to large radii.

We consider ionizing sources distributed within a characteristic radius r_0, surrounded by a dense gas envelope. From the Larson–Penston-like envelope profile shown in Figure 9, the gas density at $r > r_0$ can be approximated as

$$n_{\rm H}(r) \simeq \frac{8.86 c_{\rm s}^2}{4\pi G m_{\rm H} r^2} \simeq 5\times10^5\ {\rm cm}^{-3} \left(\frac{T}{7\times10^3\ {\rm K}}\right)\left(\frac{r}{1\ {\rm pc}}\right)^{-2}. \quad \text{(A1)}$$

For this density profile, we define the ionization radius $r_{\rm ion}$ by balancing the ionizing photon emissivity $\Phi_{\rm ion}$ with the total recombination rate between r_0 and $r_{\rm ion}$:

$$\begin{aligned}\Phi_{\rm ion} &= \int_{r_0}^{r_{\rm ion}} 4\pi r^2 dr\, \alpha_{\rm B} n_{\rm H}(r)^2 \\ &= \Phi_{\rm crit}(r_0)\left(1-\frac{r_0}{r_{\rm ion}}\right). \end{aligned} \tag{A2}$$

Here, $\alpha_{\rm B}$ is the case-B recombination coefficient. For an ionized-gas temperature of $T_{\rm II} = 10^4$ K, we adopt $\alpha_{\rm B} = 2.6\times10^{-13}$ cm^3 s^{-1}. The critical ionizing photon emissivity is

$$\begin{aligned}\Phi_{\rm crit}(r_0) &\equiv \frac{8.86^2\alpha_{\rm B}c_{\rm s}^4}{4\pi G^2 m_{\rm H}^2 r_0} \\ &\simeq 2.4\times10^{55}\ {\rm s}^{-1}\left(\frac{r_0}{1\ {\rm pc}}\right)^{-1}\left(\frac{T}{7\times10^3\ {\rm K}}\right)^2. \end{aligned} \tag{A3}$$

This is the ionizing photon emissivity required to balance all recombinations outside r_0 in an r^{-2} envelope, corresponding to the limit $r_{\rm ion}\to\infty$. For $\Phi_{\rm ion} < \Phi_{\rm crit}$, the ionized region remains finite, with

$$r_{\rm ion} = \frac{r_0}{1-\Phi_{\rm ion}/\Phi_{\rm crit}(r_0)}, \tag{A4}$$

whereas no finite equilibrium ionization radius exists for $\Phi_{\rm ion} \geq \Phi_{\rm crit}$.

We next consider a stellar population within a region of radius $\sim r_0$ consisting of $\sim 10^3$ stars with masses of $\sim 100\,{\rm M}_\odot$, corresponding to a total stellar mass of $\sim 10^5\,{\rm M}_\odot$. Assuming a luminosity of $\sim 0.5L_{\rm Edd}$ and an effective temperature of $T_{\rm eff}\sim 10^5$ K for each massive star, the total ionizing photon emissivity is approximately

$$\Phi_{\rm ion} \sim 10^{54}\ {\rm s}^{-1}. \tag{A5}$$

The ratio to the critical value is then

$$\frac{\Phi_{\rm ion}}{\Phi_{\rm crit}} \simeq 0.04\left(\frac{\Phi_{\rm ion}}{10^{54}\ {\rm s}^{-1}}\right)\left(\frac{r_0}{1\ {\rm pc}}\right)\left(\frac{T}{7\times10^3\ {\rm K}}\right)^{-2}. \tag{A6}$$

For $r_0 \sim 1$ pc, we therefore obtain $\Phi_{\rm ion} < \Phi_{\rm crit}$, and the ionized region remains close to r_0. For example, at $r_0 = 1$ pc,

$$r_{\rm ion} \simeq 1.04\, r_0. \tag{A7}$$

The ionized region therefore extends only slightly beyond the stellar distribution.

This estimate assumes static ionization equilibrium, a spherically symmetric Larson–Penston-like envelope, and a spatially averaged distribution of ionizing sources. Nevertheless, the high recombination rate in the dense r^{-2} envelope confines the ionized region close to the stellar distribution, making it difficult for ionizing radiation from the surrounding $\sim 100\,{\rm M}_\odot$ stars to affect the gas reservoir far beyond the pc scale. Photoionization feedback from these stars is therefore unlikely to significantly suppress the gas supply from larger scales and terminate accretion onto the most massive stars.